Geochimica et Cosmochimica Acta 388 (2025) 236–252

Contents lists available at ScienceDirect

Geochimica et Cosmochimica Acta

journal homepage: www.elsevier.com/locate/gca

Quantifying mass-dependent isotope fractionation and nuclear field shift effects for the light rare Earth elements in hydrous systems

Mark Nestmeyer [a,*], Alex J. McCoy-West [a,b]

[a] IsoTropics Geochemistry Laboratory, Earth and Environmental Science, James Cook University, Townsville 4811, Australia
[b] Economic Geology Research Centre, James Cook University, Townsville 4811, Australia

ARTICLE INFO

Associate editor: Xiandong Liu

Keywords:
rare Earth elements
First principles
Nuclear field shift
Stable isotope fractionation

ABSTRACT

The improving sensitivity of mass-spectrometers has opened the potential of using stable isotope signatures of the rare Earth elements (REE) as geochemical tracers. However, thus far only limited studies have utilised REE stable isotopes, despite resolvable variations having been observed in a range of systems. An interesting but poorly explored area remains variations in aqueous environments across a range of temperatures including seawater, marine sediments, ion adsorption deposits or hydrothermal systems. Furthermore, the magnitudes and competing effects of mass-dependent isotope fractionation and mass-independent nuclear field shift effects, which can be significant factor for heavy elements especially at high temperatures, remain poorly understood.

To contribute to a holistic understanding of REE isotope signatures, we calculated reduced partition function ratios (as $10^3 ln\beta$) for mass-dependent and nuclear field shift effects for aqueous La, Ce, and Nd complexes from first principles. Theoretical calculations were compared with experimental data, and this demonstrates that calculations involving a combination of two explicit hydration shells and additional implicit solvation effects are required to accurately describe the coordination and molecular vibrations of aqueous complexes. This data was then combined with speciation modelling of seawater and hydrothermal fluids to assess isotope fractionation in hydrous systems. The predicted magnitude of isotope fractionation is significant in low (T = 25 °C) temperature systems ($\Delta^{139/138}La_{Max\text{-}Min}$ = 0.20 ‰, $\Delta^{142/140}Ce_{Max\text{-}Min}$ = 0.33 ‰, $\Delta^{146/144}Nd_{Max\text{-}Min}$ = 0.34 ‰) and remains above currently achievable analytical uncertainties even at high (T = 500 °C) temperatures (±0.015 ‰ for $\delta^{146/144}$Nd; ±0.040 ‰ for $\delta^{142/140}$Ce). Unless oxidation occurs, which is only relevant for Ce in terrestrial environments, nuclear field shift effects are negligible even at temperatures up to 500 °C. The large difference in nuclear charge radius between ^{140}Ce and ^{142}Ce strongly enriches the lighter Ce isotope in the higher oxidation state ($10^3 ln\beta_{Ce(IV)\text{-}Ce(III)} = -0.45$ at 25 °C) which almost completely cancels out the opposing mass-dependent effect ($10^3 ln\beta_{Ce(IV)\text{-}Ce(III)} = +0.46$ at 25 °C). This means that variations in $\delta^{142/140}$Ce isotope signatures cannot easily be related to oxidation in ancient or recent environments.

1. Introduction

The rare Earth elements (REE) are a group of elements that consists of the lanthanides, Sc, and Y, which are of interest due to their subtle chemical differences and unique properties. The behaviour of REE in hydrous systems like seawater and rivers has been extensively investigated to understand their geochemical cycling and major sinks and sources (Elderfield, 1997; Pease and Rollinson, 2021). Despite their importance, so far, most work has focused on REE patterns and their radiogenic isotopes. For example, radiogenic ε^{143}Nd can be used to assess river and sea water mixing while Ce and Eu anomalies in sediments are used to assess paleoenvironmental redox conditions and hydrothermal sources, respectively (Danielson et al., 1992; German and Elderfield, 1990; Lacan and Jeandel, 2005; Tostevin, 2021; Vance and Burton, 1999). However, with the improving sensitivity of mass spectrometers, and renewed interested in REE due to accelerating industrial demand, the application of stable REE isotopes will become of increasing interest in the future. To date, a slowly expanding collection of studies have exploited light REE (LREE) stable isotopes (Bai, J.-H. et al., 2023; Bai et al., 2024; Hu et al., 2021; Hu et al., 2023; Nakada et al., 2013b) or Ce (Bonnand et al., 2020; Li et al., 2023a; Liu et al., 2023; Nakada et al., 2016; Pourkhorsandi et al., 2021) and Nd separately (Bai, J. et al., 2023;

* Corresponding author.
E-mail address: mark.nestmeyer@my.jcu.edu.au (M. Nestmeyer).

https://doi.org/10.1016/j.gca.2024.10.007
Received 26 May 2024; Accepted 7 October 2024
Available online 15 October 2024

Bothamy and Galy, 2021; Liu et al., 2018; McCoy-West et al., 2021; McCoy-West et al., 2017, 2020a; McCoy-West et al., 2020b; McCoy-West et al., 2022) mostly in high temperature environments and have observed limited but resolvable mass dependent isotope variations, thus their remains great potential to improve our understanding of REE mobilisation using stable isotope signatures.

Mobility and solubility of REE depends on their aqueous speciation which is controlled by the availability of ligands, pH, and temperature and is important to understand geochemical cycles (Stumm, 1987). Contribution of the REE to the ocean through hydrothermal vents and riverine runoff provide the major sources of REE, while the formation of Fe-Mn sediments on the ocean floor is the largest sink of REE in the marine environment in both the past and present (Sholkovitz et al., 1994; Sun et al., 2018; Turekian, 1977). Furthermore, remobilisation of REE through complexation with for example fluoride ligands is a significant mechanism in subaerial hydrothermal systems that can lead to ore deposit formation (Migdisov et al., 2016). Likewise, sorption onto clay minerals has been identified as a process for the formation ion adsorption-type REE deposits (Sanematsu et al., 2016). Since aqueous REE species show different stabilities and reactivities for adsorption onto minerals, understanding the isotope fractionation between different aqueous species is crucial to be able use stable isotopes as tracers (Li et al., 2022; Nakada et al., 2017; Nakada et al., 2013b). The range of different species that a metal can form in an aqueous solution, all represent different bonding environments and therefore, metal isotopes will fractionate to varying extents between different coexisting species as shown for numerous elements in previous studies (Black et al., 2011; Fujii et al., 2023; Fujii et al., 2014; Li et al., 2009; Sherman, 2013; Yang et al., 2015; Zhang and Shi, 2022; Zhao et al., 2021). According to the principles of mass-dependent isotope fractionation at equilibrium, heavier isotopes concentrate in bonding environments with shorter bonds, lower coordination numbers, and higher oxidation states. However, elements with heavier masses like the REE will exhibit a smaller magnitude of isotope fractionation, due to their smaller relative mass differences (Schauble, 2004).

Isotope fractionation during ligand exchange and oxidation reactions is also driven by mass independent effects (e.g. nuclear spin effect, anharmonic vibration correction), among which only nuclear field shift (NFS) effects are considered significant (Fujii et al., 2009; Yang and Liu, 2016). Nuclear field shift is proportional to the difference in nuclear charge radii between two isotopes and is associated with atomic mass but does not simply correlate with the number of nuclei (Yang and Liu, 2016). Nuclear field shift effects have been observed experimentally in various exchange reactions and agree with theoretical calculations from first principles (Abe et al., 2008; Fujii et al., 2012; Wiederhold et al., 2010). The magnitude of isotope fractionation induced by NFS increases rapidly with increasing mass and can dominate isotope fractionation in heavy elements such as Eu and Tl (Fujii et al., 2012; Schauble, 2023), especially when changes in oxidation state occur. Also, in high temperature regimes (i.e. magma chambers or hydrothermal systems) given the magnitude of mass dependent isotope fractionation scales proportional to $1/T^2$ (Bigeleisen and Mayer, 1947), whereas NFS effects are only proportional to 1/T, therefore NFS effects become more significant with increasing temperature (Fujii et al., 2009).

Currently, however, for the REE the magnitude of both mass-dependent and mass-independent isotope effects are not fully understood, although a better understanding is crucial for accurate interpretations of stable isotope signatures. This study uses a computational quantum chemical approach to quantify the potential of using light REE stable isotope signatures as tracers of chemical cycling and ore deposit formation. We have calculated reduced partition function ratios (β-factors) for a range of aqueous species of La, Ce, and Nd for the isotope ratios $^{139}La/^{138}La$, $^{142}Ce/^{140}Ce$, $^{146}Nd/^{144}Nd$, and $^{148}Nd/^{144}Nd$. Here, we have focused on just the light REE (La-Nd) because they show a similar ninefold coordination structures in aqueous solutions based on synchrotron observations, with bonding environment beginning to shift towards eightfold coordination for REE heavier than Sm (Ishiguro et al., 2002; Persson et al., 2008). Given that Pr has only one stable isotope (^{141}Pr) it has been omitted from this study. The obtained β-factors were used to model the isotope fractionation between aqueous species for hydrous systems at variable fluid conditions. To assess the significance of mass-independent isotope fractionation effects, nuclear field shift effects (NFS) were computed for variable aqueous complexes and oxidation states for REE elements and modelled over a temperature range up to 500 °C. This dataset is then used to discuss the implications for REE isotope fractionations and cycling in a range of hydrous environments.

2. Methodology

2.1. Mass dependent isotope fractionation

To quantify isotope fractionation between aqueous REE species we calculated reduced partition function ratios (β-factors) from first principles. Vibrational frequencies of optimised aqueous REE complexes were calculated with density functional theory (DFT) in ORCA v.5.0.1 (Neese, 2011) using a cluster approach. Firstly, one hydration shell of the aqueous complexes was optimised and then 16 additional water molecules were added and again optimised (additional water molecules moved to the third hydration shell). The number of water molecules in the first hydration shell were taken from Zhang and Yan (2022) who investigated the molecular structure for La complexes with the major aqueous anion ligands Cl^-, F^-, SO_4^{2-}, CO_3^{2-}, and HCO_3^- through molecular dynamic simulations. The conductor-like polarizable continuum model (CPCM) was applied for additional implicit solvation effects in water. The PBE0 hybrid functional was used for all calculations (Adamo and Barone, 1999). The def2 split-valence basis set was used for lighter elements O, H, Cl, S, C, and F (Weigend and Ahlrichs, 2005). The def2 triple-zeta basis set was used for REE valence electrons together with a Stuttgart-Dresden effective core potential (ECP) (Dolg et al., 1989) for core electrons. A comparison of variable computational setups and why the models described here are suitable to predict isotope fractionation is discussed later in the article. Convergence tolerance for self-consistent field (SCF) and geometry optimisation were set to $1.0E^{-9}$ Eh and $2.0E^{-7}$ Eh, respectively. A denser integration grid 'defgrid3' was used for a more precise calculation. Complexes with unpaired valence electrons (Ce^{3+}, Nd^{3+}) were treated with unrestricted Kohn-Sham (UKS) wavefunctions. The Split-RI-J coulomb approximation (Neese, 2003) has been used with the def2/J auxiliary basis set (Weigend, 2006). Isotope masses for La, Ce, and Nd were taken from Meija et al. (2016). Yielded vibrational frequencies were used to calculate reduced partition function ratios for mass-dependent isotope fractionation (β_{MD}) from 0 ° to 500 °C according to the equation (Bigeleisen and Mayer, 1947; Urey, 1947):

$$\beta_{MD} = \prod_{i=1}^{N} \frac{u_i}{u_i'} \frac{\exp(-u_i/2)/(1-\exp(-u_i))}{\exp(-u_i'/2)/(1-\exp(-u_i'))} \quad (1)$$

with

$$u_i = \frac{hc\omega_i}{kT} \quad (2)$$

where h is Planck's constant, c is speed of light, k is Boltzmann constant, T is absolute temperature, ω_i is the i^{th} of $3N$-6 vibrational frequencies (where N = number of atoms in complex), and u' refers to the lighter isotope. No imaginary frequencies were observed which confirms a successful geometry optimisation. For most anion complexes, the addition of 16 water molecules to the first hydration shell made some water molecules move to a third hydration shell indicating two fully occupied explicit hydration shells. Vibrational frequencies were visualised in AVOGADRO (Hanwell et al., 2012). The REE-O stretch was identified by

a 'breathing'-like vibration of the first hydration shell along REE-O bonds and has been compared with experimental data to validate the computational setup (Rudolph and Irmer, 2020). Reduced partition function ratios are expressed as $10^3 ln\beta$ which allows us to estimate the difference in isotopic composition between two phases (Δ) in δ-notation relative to a widely used reference material:

$$10^3 ln\alpha_{A-B} = 10^3 ln\beta_A - 10^3 ln\beta_B \quad (3)$$

and

$$10^3 ln\alpha_{A-B} \approx \delta^i REE_A - \delta^i REE_B = \Delta^i REE_{A-B} \quad (4)$$

where REE is either La, Ce or Nd, *i* refers to an isotope ratio, and A and B represent two phases in isotopic equilibrium.

2.2. Aqueous speciation modelling

Aqueous speciation modelling was performed in PHREEQC (Parkhurst and Appelo, 2013) with the Thermoddem database v1.10 (Blanc et al., 2012) which allows modelling of REE speciation at temperatures up to 300 °C. Oxide species (e.g. $REEO^+$, $REEO_2^-$) have been excluded from the database because oxygen atoms kept on scavenging hydrogens from water molecules during geometry optimisation resulting in hydroxide complexes. The behaviour of two different water

Table 1
Calculated $10^3 ln\beta_{MD}$ (MD = Mass Dependent) values for aqueous La, Ce, and Nd complexes.

Species	Temperature (°C)							
	0	25	50	100	200	300	400	500
Lanthanum Species								
$La(H_2O)_9(H_2O)_{16}^{3+}$	0.620	0.524	0.448	0.339	0.213	0.146	0.106	0.081
$La(H_2O)_8(H_2O)_{16}^{3+}$	0.649	0.549	0.470	0.355	0.223	0.153	0.111	0.084
$LaCl(H_2O)_8(H_2O)_{16}^{2+}$	0.589	0.497	0.425	0.321	0.201	0.138	0.100	0.076
$LaCl(H_2O)_7(H_2O)_{16}^{2+}$	0.656	0.556	0.477	0.363	0.230	0.159	0.116	0.089
cis-$LaCl_2(H_2O)_6(H_2O)_{16}^{+}$	0.574	0.485	0.416	0.315	0.199	0.136	0.099	0.076
trans-$LaCl_2(H_2O)_6(H_2O)_{16}^{+}$	0.558	0.471	0.403	0.305	0.191	0.131	0.095	0.072
mer-$LaCl_3(H_2O)_5(H_2O)_{16}$	0.501	0.422	0.361	0.272	0.170	0.116	0.084	0.064
fac-$LaCl_3(H_2O)_5(H_2O)_{16}$	0.535	0.451	0.386	0.291	0.182	0.125	0.091	0.069
$LaF(H_2O)_8(H_2O)_{16}^{2+}$	0.684	0.579	0.496	0.376	0.236	0.162	0.118	0.090
cis-$LaF_2(H_2O)_6(H_2O)_{16}^{+}$	0.684	0.578	0.495	0.374	0.235	0.161	0.117	0.089
trans-$LaF_2(H_2O)_6(H_2O)_{16}^{+}$	0.633	0.534	0.457	0.345	0.216	0.148	0.107	0.081
mer-$LaF_3(H_2O)_5(H_2O)_{16}$	0.715	0.605	0.518	0.392	0.246	0.169	0.123	0.093
fac-$LaF_3(H_2O)_5(H_2O)_{16}$	0.692	0.586	0.502	0.380	0.239	0.164	0.119	0.091
$LaSO_4(H_2O)_7(H_2O)_{16}^{+}$	0.615	0.519	0.444	0.335	0.210	0.144	0.105	0.079
$LaCO_3(H_2O)_8(H_2O)_{16}^{+}$	0.620	0.524	0.449	0.340	0.214	0.147	0.107	0.081
$LaHCO_3(H_2O)_7(H_2O)_{16}^{2+}$	0.617	0.522	0.448	0.340	0.215	0.148	0.108	0.083
$LaOH(H_2O)_8(H_2O)_{16}^{2+}$	0.658	0.558	0.479	0.364	0.231	0.160	0.117	0.090
cis-$La(OH)_2(H_2O)_6(H_2O)_{16}^{+}$	0.563	0.476	0.407	0.308	0.193	0.132	0.096	0.073
trans-$La(OH)_2(H_2O)_6(H_2O)_{16}^{+}$	0.587	0.497	0.426	0.322	0.203	0.139	0.101	0.077
mer-$La(OH)_3(H_2O)_5(H_2O)_{16}$	0.545	0.460	0.394	0.298	0.187	0.128	0.093	0.071
fac-$La(OH)_3(H_2O)_5(H_2O)_{16}$	0.617	0.523	0.449	0.341	0.216	0.148	0.108	0.082
$LaHS(H_2O)_8(H_2O)_{16}^{2+}$	0.483	0.407	0.348	0.262	0.164	0.112	0.082	0.062
Cerium Species								
$Ce(H_2O)_9(H_2O)_{16}^{3+}$	1.069	0.904	0.774	0.587	0.370	0.254	0.186	0.142
$Ce(H_2O)_8(H_2O)_{16}^{3+}$	1.102	0.931	0.796	0.601	0.377	0.258	0.187	0.142
$Ce(H_2O)_9(H_2O)_{16}^{4+}$	1.614	1.368	1.174	0.891	0.563	0.387	0.282	0.215
$CeCl(H_2O)_8(H_2O)_{16}^{2+}$	1.049	0.888	0.760	0.576	0.363	0.250	0.183	0.139
$CeCl(H_2O)_7(H_2O)_{16}^{2+}$	1.094	0.924	0.791	0.597	0.375	0.257	0.187	0.142
$CeCl_2(H_2O)_6(H_2O)_{16}^{+}$	0.954	0.805	0.688	0.519	0.325	0.222	0.161	0.123
$CeCl_3(H_2O)_5(H_2O)_{16}$	0.988	0.835	0.715	0.542	0.342	0.235	0.172	0.131
$CeF(H_2O)_8(H_2O)_{16}^{2+}$	1.340	1.136	0.975	0.744	0.469	0.323	0.236	0.180
$CeF_2(H_2O)_6(H_2O)_{16}^{+}$	1.197	1.012	0.866	0.655	0.412	0.283	0.206	0.156
$CeF_3(H_2O)_5(H_2O)_{16}$	1.317	1.115	0.956	0.725	0.457	0.314	0.229	0.174
$CeSO_4(H_2O)_7(H_2O)_{16}^{+}$	1.345	1.137	0.974	0.737	0.463	0.318	0.231	0.176
$CeCO_3(H_2O)_8(H_2O)_{16}^{+}$	1.059	0.894	0.765	0.578	0.362	0.248	0.180	0.137
$CeHCO_3(H_2O)_7(H_2O)_{16}^{2+}$	1.220	1.034	0.887	0.674	0.427	0.295	0.216	0.165
$CeOH(H_2O)_8(H_2O)_{16}^{2+}$	1.153	0.976	0.836	0.633	0.398	0.273	0.199	0.151
$Ce(OH)_2(H_2O)_6(H_2O)_{16}^{+}$	1.110	0.940	0.807	0.612	0.386	0.265	0.193	0.147
$Ce(OH)_3(H_2O)_5(H_2O)_{16}$	1.142	0.967	0.830	0.630	0.397	0.273	0.199	0.151
$CeHS(H_2O)_8(H_2O)_{16}^{2+}$	0.999	0.844	0.722	0.545	0.342	0.234	0.171	0.130
Neodymium Species								
$Nd(H_2O)_9(H_2O)_{16}^{3+}$	1.062	0.898	0.769	0.581	0.365	0.250	0.182	0.138
$Nd(H_2O)_8(H_2O)_{16}^{3+}$	1.194	1.010	0.865	0.655	0.412	0.282	0.205	0.156
$NdCl(H_2O)_8(H_2O)_{16}^{2+}$	1.086	0.918	0.786	0.594	0.373	0.256	0.186	0.141
$NdCl(H_2O)_7(H_2O)_{16}^{2+}$	1.102	0.931	0.797	0.603	0.379	0.260	0.189	0.144
$NdCl_2(H_2O)_6(H_2O)_{16}^{+}$	0.990	0.835	0.715	0.540	0.339	0.232	0.169	0.128
$NdCl_3(H_2O)_4(H_2O)_{16}$	0.916	0.773	0.661	0.498	0.312	0.214	0.155	0.118
$NdF(H_2O)_8(H_2O)_{16}^{2+}$	1.318	1.117	0.959	0.729	0.460	0.317	0.231	0.176
$NdF_2(H_2O)_6(H_2O)_{16}^{+}$	1.167	0.987	0.846	0.641	0.404	0.277	0.202	0.153
$NdF_3(H_2O)_5(H_2O)_{16}$	1.240	1.049	0.898	0.680	0.428	0.294	0.215	0.163
$NdSO_4(H_2O)_7(H_2O)_{16}^{+}$	1.103	0.933	0.799	0.606	0.382	0.263	0.192	0.146
$NdCO_3(H_2O)_7(H_2O)_{16}^{+}$	1.188	1.005	0.862	0.653	0.412	0.284	0.207	0.158
$NdHCO_3(H_2O)_7(H_2O)_{16}^{2+}$	1.123	0.949	0.812	0.614	0.386	0.264	0.192	0.146
$NdOH(H_2O)_8(H_2O)_{16}^{2+}$	1.124	0.951	0.815	0.617	0.389	0.267	0.194	0.148
$Nd(OH)_2(H_2O)_6(H_2O)_{16}^{+}$	1.119	0.948	0.812	0.616	0.388	0.266	0.194	0.147
$Nd(OH)_3(H_2O)_4(H_2O)_{16}$	1.139	0.967	0.831	0.634	0.403	0.279	0.205	0.157
$NdHS(H_2O)_8(H_2O)_{16}^{2+}$	0.993	0.840	0.720	0.546	0.345	0.237	0.173	0.132

compositions (Table S1), modern seawater, and hydrothermal fluid has been investigated with solution parameters and elemental concentrations taken from the MARHYS database (Diehl and Bach, 2020).

Simulations of the simplified seawater were performed over a pH range of 2–12 at a constant temperature of 25 °C. Speciation in a hydrothermal system was simulated over a temperature range of 0 ° – 300 °C and a starting pH of 5.13. During the simulation, the pH was kept between 4.67 and 5.55 by adding HNO_3. Nitric acid was chosen over HCl to keep the chloride concentration in the solution constant.

The speciation models were combined with β-factors from *2.1* (Table 1) to calculate the isotopic composition of each species using the equation:

$$\delta^i REE_i = \delta^i REE_{bulk} - \frac{\sum_{j \neq i}(10^3 ln\beta_j - 10^3 ln\beta_i) \times f_j}{f_i} \quad (5)$$

where δ^iREE is the isotopic composition of the i^{th} species of REE in solution, f_i is the fraction of the species i, f_j is the fraction of all other species, and REE = either La, Ce or Nd. A bulk composition of 0 ‰ was assumed for all simulations because we are only interested in variations between the isotopic compositions of different species. Given that mass-dependent isotope fractionation in equilibrium is temperature dependent, an individual $10^3 ln\beta$ value for each temperature step of 3 °C (100 steps) was calculated by interpolation of the $10^3 ln\beta$ values from Table 1.

2.3. Nuclear field shift effects

To quantify the magnitude of nuclear field shift (NFS) effects, we computed $10^3 ln\beta_{NFS}$ for REE-species with relativistic total energy calculations using the Dirac-Hartree-Fock (DHF) method in DIRAC v.22.0 (Saue et al., 2020). Because REE are heavy elements (Z > 40), inner-shell electrons move with a velocity close to light speed to avoid falling into the nucleus. This phenomenon causes further relativistic effects which must be considered, given neglecting these relativistic effects will produce inaccurate electronic structures for heavy elements. Whereas vibrational frequencies mostly depend on the motion and mass of the nucleus as well as interatomic forces which are largely non-relativistic properties. Therefore, relativistic calculations are only used here for NFS calculations. REE-species include aqueous complexes but also metallic REE^0 and ionic REE^{3+} and REE^{4+}. The nuclear field shift effect is defined as:

$$10^3 ln\beta_{NFS} = 10^3 \times \frac{(E[REEX] - E[REE'X]) - (E[REEY] - E[REE'Y])}{kT} \quad (6)$$

where E is the total energy of a species. REE' and REE are the light and heavy isotopes, respectively, and X represents the different species (Fujii et al., 2009). Phase Y represents a perfect gas of La^0 or Ce^0. The total energies of REE-species were calculated using the coordinates of the DFT-optimised species with only one hydration shell. The effect of additional hydration shells on the accuracy of nuclear filed shift effects has not been thoroughly investigated in previous studies. Here, we had convergence problems with large clusters (two hydration shells) in DIRAC. Experimental data of REE in aqueous systems are required to assess the computational setup for relativistic calculations in future studies. Energies were calculated using the exact two component Hamiltonian (X2C). For light elements (H, O, Cl, C, S, and F), the def2-svp basis set was used whereas a relativistic core-valence triple-zeta Dyall basis set (Gomes et al., 2010) was used for REE elements. A non-relativistic basis set was used for lighter elements because relativistic effects are negligible in light elements (Christiansen et al., 1985). Energies were calculated using uncontracted basis sets. To obtain the energy differences for isotope dependent nuclear radii, the root mean square nuclear charge radius ($< r^2 >$) was specified for REE isotopes through the gaussian exponent ξ which is defined as (Visscher and Dyall, 1997):

$$\xi = \frac{3}{2 < r^2 >} \quad (7)$$

The values for $< r^2 >$ were taken from Angeli and Marinova (2013). Electron configurations used for atomic and ionic REE elements are given in Table S2. The total reduced partition function ratio ($10^3 ln\beta_{TOT}$) can then be calculated through the summation of the β-factors for mass dependent and nuclear field shift effects (Bigeleisen, 1998):

$$10^3 ln\beta_{TOT} = 10^3 ln\beta_{MD} + 10^3 ln\beta_{NFS} \quad (8)$$

3. Results

3.1. Mass-dependent isotope fractionation

The optimised aqueous species of La, Ce, and Nd were visualised in VESTA (Momma and Izumi, 2011) and are shown in Fig. 1. Calculated $10^3 ln\beta_{MD}$ values are given in Table 1, S3. A change in coordination number between Ce^{3+} and Ce^{4+} was not observed despite atomic size decreasing with removal of the 4f electron. Isotope fractionation between aqueous species decreases nearly linearly with increasing temperature proportional to $1/T^2$ (Fig. 2). The $10^3 ln\beta$ values for $^{139}La/^{138}La$ are between 0.41 and 0.60 ($\Delta^{139/138}La_{1000ln\beta} = 0.18$) at 298 K (25 °C) while $10^3 ln\beta$ for $^{148}Nd/^{144}Nd$ reaches values of 1.56 to 2.13 ($\Delta^{148/144}Nd_{1000ln\beta} = 0.58$). The maximum isotope fractionation between trivalent Ce complexes is $\Delta^{142/140}Ce_{1000ln\beta} = 0.33$ while difference in $10^3 ln\beta$ between hydrated Ce^{3+} and Ce^{4+} is 0.46 at 25 °C with Ce^{4+} being isotopically heavier. Similar to tetravalent Ce complexes, maximum isotope fractionation for the $^{146}Nd/^{144}Nd$ ratio is 0.34 (Table 1). Light REE-oxygen bonds generally become smaller with increasing atomic mass. For example, La-O length in hydrated La^{3+} is 2.60 Å and decreases to 2.56 Å for Ce-O and 2.52 Å for Nd-O (Table S6). Isotope fractionation for some geometric isomers of chloride, fluoride, and hydroxide complexes of La were also quantified. The geometric isomers are illustrated in Fig. S1 and mass-dependent isotope fractionation between the complexes is shown in Fig. S2 and Table 1. The magnitude of isotope fractionation varies from a minimum of 0.014 ‰ between *cis*-, and *trans*-$LaCl_2$ complexes to a maximum of 0.063 ‰ between *mer*-, and *fac*- La $(OH)_3$ complexes at 25 °C.

3.2. Speciation modelling

According to the Thermoddem database utilised here, the speciation of light REE in aqueous solution is very similar as shown in Fig. 3. Aqueous species that account for < 1 % have been excluded ($REECl_3$, $REECl_4^-$, $REEF_2^+$, $REEF_3$, $REEF_4^-$, $REEH_2PO_4^{2+}$). At room temperature, REE form carbonate complexes with increasing pH reaching a proportion of > 90 % in the seawater model (Fig. 3A-C). Free REE^{3+} and $REESO_4^+$ are the dominant aqueous species at lower pH < 6 (Fig. 3A-C). The relative shifts in isotopic composition around pH 7 and 11 are due to the progressive increase in CO_3^{2-} and OH^- complexes, respectively (Fig. 3D-F), resulting in the composition of these complexes shifting closer to the bulk composition (i.e. 0 ‰).

Speciation in a simplified hydrothermal system is considerably different and clearly varies with fluid temperature (Fig. 4A-C). Higher temperatures promote the formation of more Cl^-- and F^-- complexes at the expense of free REE^{3+} and SO_4^{2-} complexes. As predicted with increasing temperature, the magnitude of isotope fractionation between aqueous species becomes smaller (Fig. 4D-F).

3.3. Nuclear field shift effects

Nuclear field shift effects for La and Ce atoms and complexes are presented in Fig. 5A, B and Table 2. Isotope fractionation effects are very small between species with identical oxidation states (REE^{3+}) but become significant when different oxidation states exist as is the case for

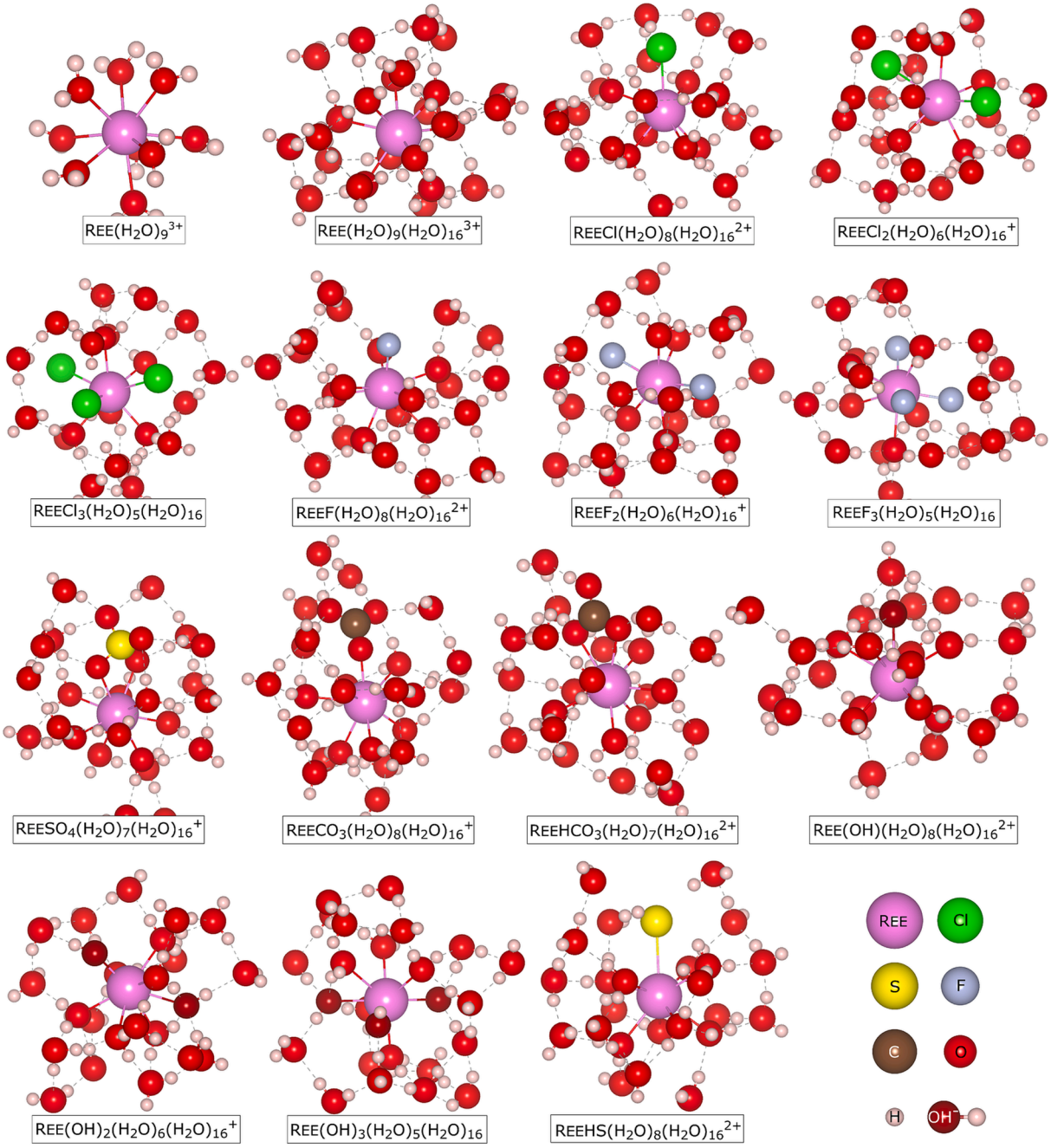

Fig. 1. Overview of optimised aqueous REE complexes including one or two explicit hydration shells per complex. For additional implicit water solvation effects, the conductor-like polarizable continuum model (CPCM) was applied.

Ce. Tetravalent species Ce^{4+} preferentially incorporate lighter isotopes relative to metallic Ce^0, whereas trivalent species Ce^{3+} preferentially incorporates heavier isotopes relative to metallic Ce^0. Additionally, the hydration of ionic REE affects the isotope fractionation with non-hydrated species being isotopically heavier (Fig. 5A). Isotope fractionation by NFS displays the characteristic proportionality to 1/T (Fig. 5).

The NFS effect for the oxidation reaction of Ce^{3+} to Ce^{4+} for all combinations of stable Ce isotopes is presented in Table S4 and illustrated in Fig. 5C. In contrast to mass-dependent isotope fractionation, the difference in nuclear charge radius leads to a large enrichment of the lighter isotope in the higher oxidation state of Ce for the $^{142}Ce/^{140}Ce$ ratio. Depending on the isotope pair considered, the magnitude of this effect varies from highly negative ($10^3 ln\beta_{Ce(IV)\text{-}Ce(III)}$ = -0.47 to -0.52 at 25 °C) when ^{142}Ce is involved, to relatively negligible ($10^3 ln\beta_{Ce(IV)\text{-}Ce(III)}$ = -0.055 to 0.003 at 25 °C) for the other isotope pairs.

4. Discussion

4.1. Evaluation of computational methods

In order to ensure reliable interpretations can be made using the mass-dependent and mass-independent isotope fractionation data herein, the robustness of the computational setups was firstly evaluated with respect to its accuracy prior to considering its implications for understanding hydrous systems.

4.1.1. Accuracy of DFT calculations

To confirm the vibrational frequencies presented herein are robust

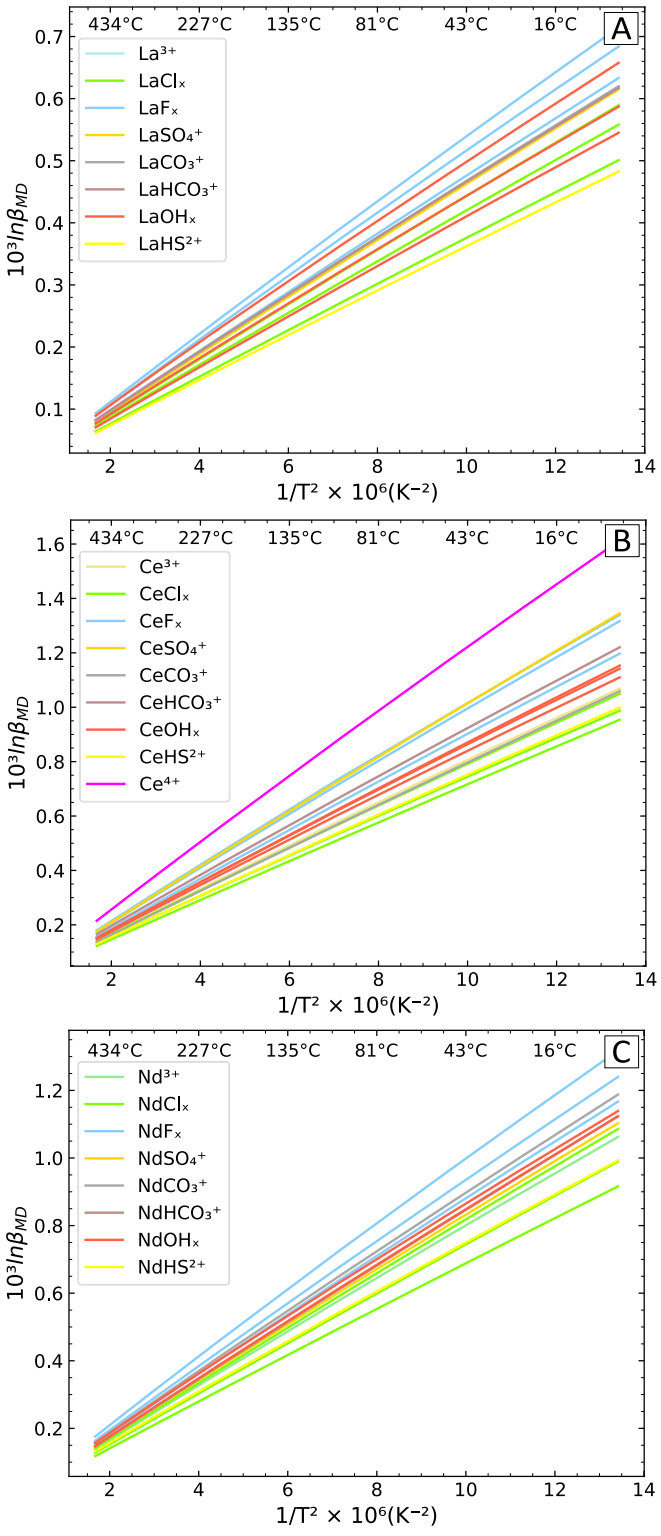

Fig. 2. Mass dependent $10^3\ln\beta$ values for a variety of aqueous species for (A) $^{139}La/^{138}La$, (B) $^{142}Ce/^{140}Ce$, and (C) $^{146}Nd/^{144}Nd$ calculated in this study. The diagrams show a clear relationship between mass-dependent isotope fractionation and $1/T^2$ and therefore a smaller fractionation between aqueous complexes at elevated temperature.

and accurate, several setups including variable basis sets and different solvation effects were tested which are presented in Table 3. The experimental La-O stretching frequency (343 cm^{-1}; Rudolph and Irmer (2020)) is poorly reproduced by using only one hydration shell to simulate solvation effects (281 cm^{-1}). The addition of a continuum model for implicit solvation effects, resulted in only a slight improvement (308 cm^{-1}). Adding a second explicit hydration shell of 14 water molecules still produced a vibrational frequency (334 cm^{-1}) slightly lower than the experimental data. Finally, adding implicit solvation effects to two explicit hydration shells allowed us to keep 16 water molecules in the second shell, which is closer to the experimental value of 18 (Naslund et al., 2000) and perfectly agrees with the 16 water molecules observed in a molecular dynamics simulation (Clavaguera et al., 2005). The def2-svp basis set shows a better performance for lighter elements, while the def2-tzvp basis set worked better for the heavy REE elements leading to a slightly better agreement with experimental vibrational frequency (318 cm-1; Table 3). A combination of these two basis sets and two explicit hydration shells together with implicit solvation effects yielded excellent agreement with experimental data for the REE-O stretching frequencies (Fig. 6, D-F, Table S5). Additionally, using a LANL2TZ basis set (Roy et al., 2008) for La with a Hay-Wadt ECP (Hay and Wadt, 1985) and a people style split valence 6-31G(d,p) basis set (Hehre et al., 1972) for H, and O, produced results similar to using def2 basis sets (Table 3). This indicates that the accuracy of calculated properties is more sensitive to changes in solvation effects than to the choice of the basis set. However, LANL basis sets are only available for La in ORCA and not for Ce, and Nd, so we have implemented def2 basis sets throughout.

Based on the calculations herein different LREE show element-specific variations in $10^3\ln\beta$ between the various complexes (Fig. 2). This can be attributed to: (1) Lanthanide contraction: a systematic decrease in REE-O bond lengths due to the shielding of an additional 4f electrons. The decrease in REE-O bond length from 2.60 Å in hydrated La^{3+} over 2.56 in Ce^{3+} to 2.52 Å in Nd^{3+} observed here (Fig. 6A-C; Table S6) is consistent with previous experimental studies (Persson et al., 2008; Rudolph and Irmer, 2020). (2) Jahn-Teller effects: the higher distortion in open shell complexes (Ce, Nd) due to additional valence electrons can also cause variation in individual geometries. Interestingly, bond lengths are generally overestimated by around 0.04 Å by calculations using two explicit hydration shells while bond lengths replicate experimental data exceptionally well when only one hydration shell plus implicit solvation effects was used (Fig. 6A-C; Table S6). Models using only one hydration shell plot within uncertainty (2 × standard deviation) of the average of published experimental data (DFT and molecular dynamics studies were omitted from the average) while bond lengths derived from calculations with two hydration shells plus implicit solvation effects fall outside this range (Fig. 6A-C). For Ce and Nd, the bond lengths generated herein are also very close to the average experimental data ($\Delta REE\text{-}O_{Exp\text{-}DFT}$ = 0.006 Å and 0.003 Å, respectively) while a small overestimation remains for La ($\Delta La\text{-}O_{Exp\text{-}DFT}$ = 0.017 Å). Given that mass-dependent isotope fractionation in equilibrium is governed only by the vibrational energies, a small inaccuracy in bond lengths calculated herein (for two hydration shells) should have no perceptible effect on the quality of our results.

Mass-dependent isotope fractionation scales with Δm/mm' where Δm is the mass difference between the two considered isotopes and mm' is the average of the two masses. This is consistent with the progressively smaller range of $10^3\ln\beta$ for $^{139}La/^{138}La$ than for $^{142}Ce/^{140}Ce$ and $^{146}Nd/^{144}Nd$, compared to $^{148}Nd/^{144}Nd$ (Fig. 2, Table 1). The smaller mass difference between the La isotopes (1 amu) makes it more challenging to resolve stable isotope fractionations and given there are no other stable La isotopes available (Fig. 7A), La is not the most prospective choice for a LREE geochemical tracer although its concentration is often the highest. Additionally, given the odd mass number of ^{139}La it is susceptible to nuclear-spin effects which are mass-independent fractionation effects (Buchachenko, 2013).

A general correlation of $10^3\ln\beta$ and the electronegativity of the bonding partner has been observed in previous studies and is commonly used as an indicator for isotope fractionation between molecules (Albarède et al., 2017; Fujii et al., 2014; Moynier et al., 2013; Zhao et al.,

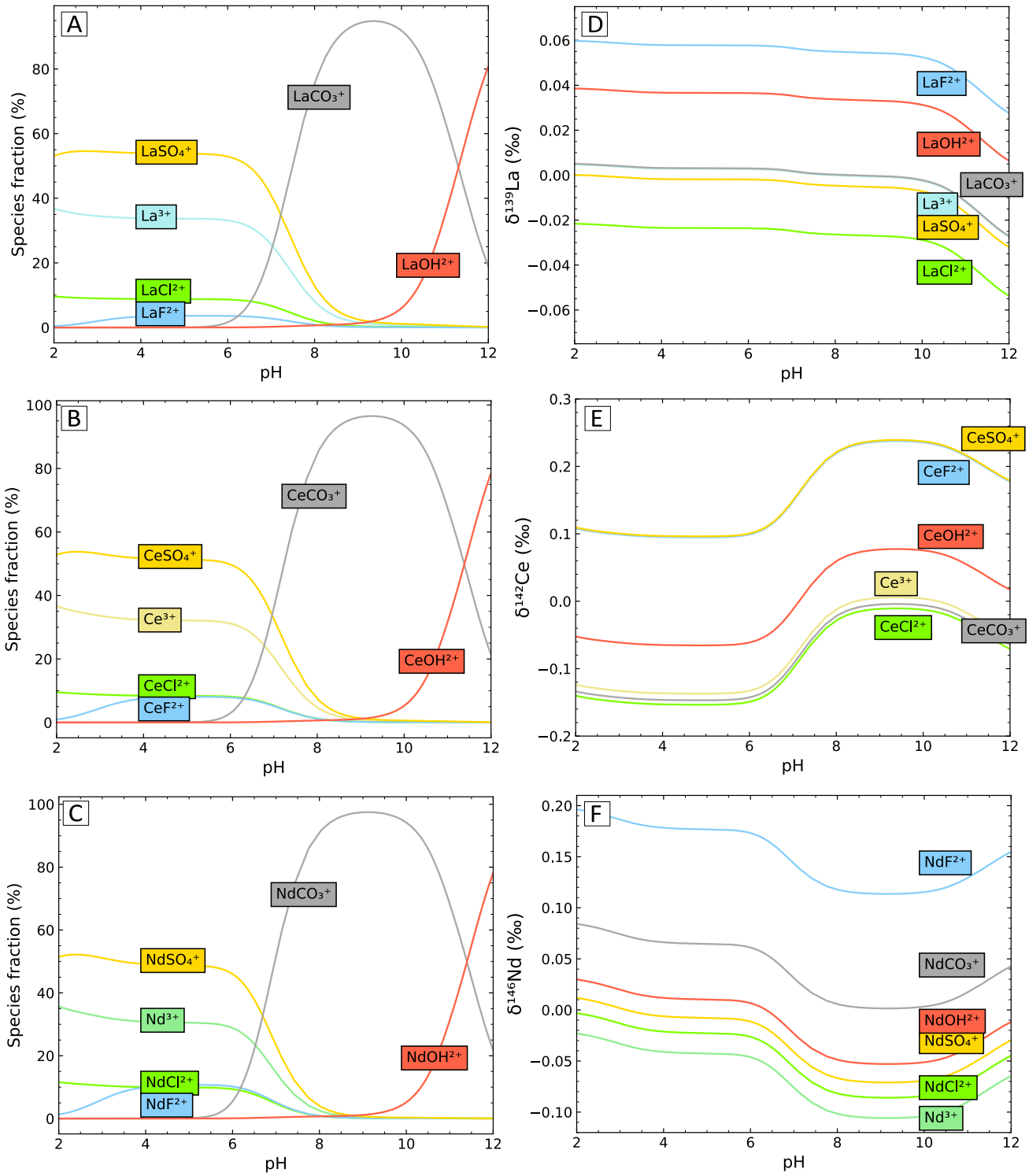

Fig. 3. (A-C) Aqueous speciation of La, Ce, and Nd in simplified modern seawater from pH 2 to 12 at 25 °C. Speciation follows the same trend for all three REE. The proportion of CO_3^{2-} complexes increases with increasing pH and reaches a proportion of > 90 %. (D-F) Isotopic composition of aqueous La, Ce, and Nd species in seawater at 25 °C.

2021). Fig. 8A-C confirms this trend for REE complexes with, for example, HS^- and Cl^- species being among the lightest complexes whereas F^- complexes are consistently the heaviest species.

4.1.2. *Evaluation of electronic structure calculations*

Relativistic and non-relativistic Hartree-Fock calculations of ground-state energies of La^0 and Ce^0 are in good agreement with previously published calculations which have used different basis sets (Fig. S3A, B). Furthermore, only negligible variations between various relativistic Dyall basis sets of double zeta and triple zeta quality (e.g. CV2Z, CV3Z, AE2Z, AE3Z) are observed (Fig. S3A, B). The computationally less expensive 2-component Hamiltonian X2C agrees well with the Dirac-Coulomb (DC) Hamiltonian (Fig. S3A, B). The model used for our $10^3 \ln\beta_{NFS}$ computations (X2C/CV3Z) approximates very well

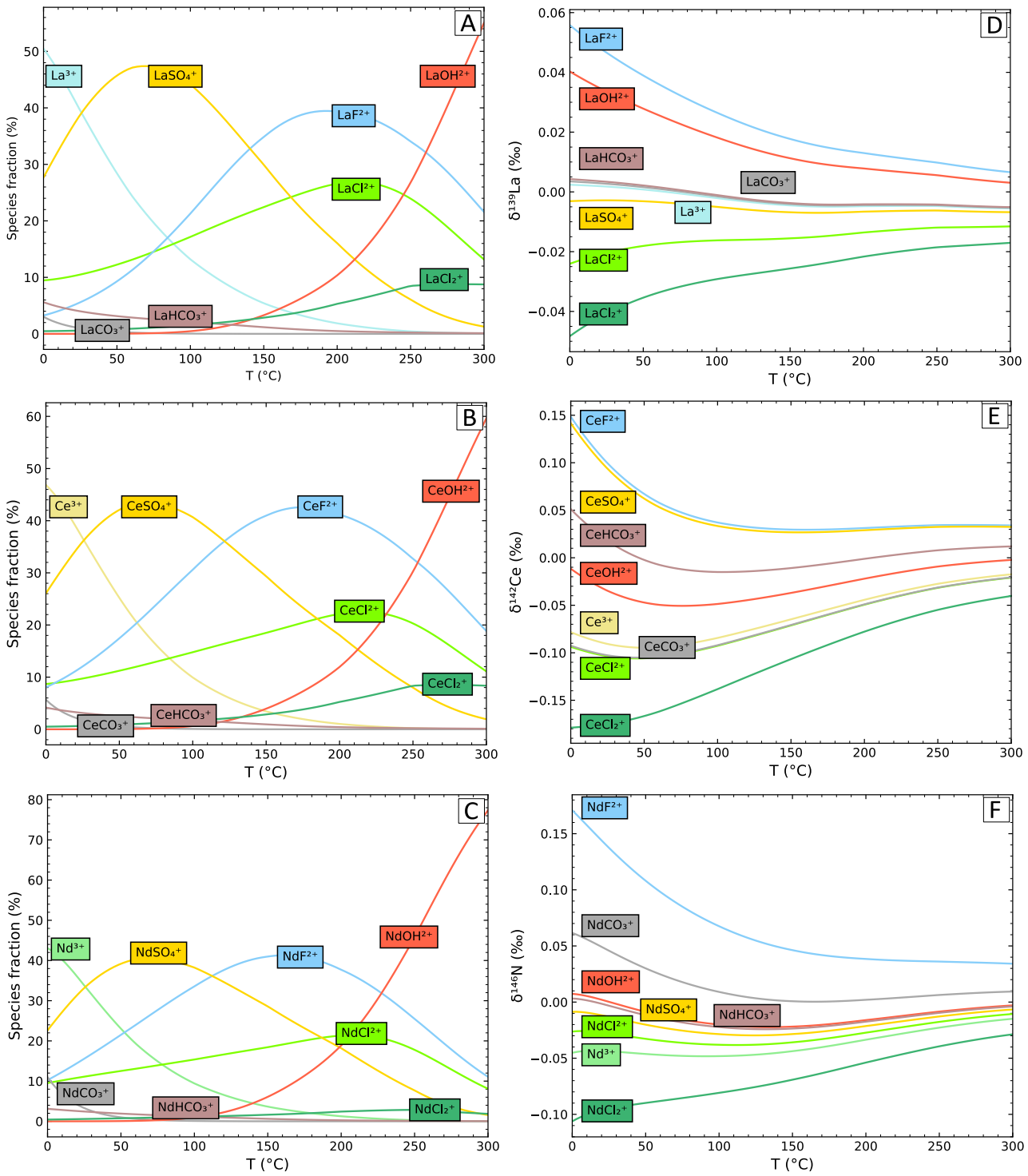

Fig. 4. (A-C) Speciation of La, Ce, and Nd in a simplified hydrothermal fluid with temperature varying from 0 ° to 300 °C. (D-F) Isotope fractionation between aqueous La, Ce, and Nd species in a hydrothermal fluid. The mass-dependent isotope fractionation decreases with a proportionality to $1/T^2$ making it more challenging to resolve isotope fractionation in high-temperature systems.

experimental data of ionisations energies of La and Ce (Table S7). A range of basis sets were tested for La^{3+} and clearly demonstrate that results from non-relativistic calculations differ significantly from relativistic calculations and therefore non-relativistic calculations are not sufficient to describe NFS effects in REE species (Fig. S4). Similar to total energy calculations (as discussed above), variations in $10^3 \ln\beta_{NFS}$ between the different relativistic Dyall basis sets are also negligible (Fig. S4). Additionally, to verify accuracy we qualitatively cross-checked our results with available isomer shifts data for REE. Isomer shifts are sensitive to the electron density at the nucleus $|\psi(0)|^2$ and have been widely studied for Sm and Eu (Brix et al., 1964; Coey, 1976; Eibschütz et al., 1972; Gerth et al., 1968). The nuclear field shift effect is also proportional to $|\psi(0)|^2$. We can refer here to Eu, and Sm because of the similar electronic structure of REE elements which are only distinguished by additional 4f or 5d electrons. Isomer shift results demonstrate that $|\psi(0)|^2$ varies only slightly between REE phases of identical

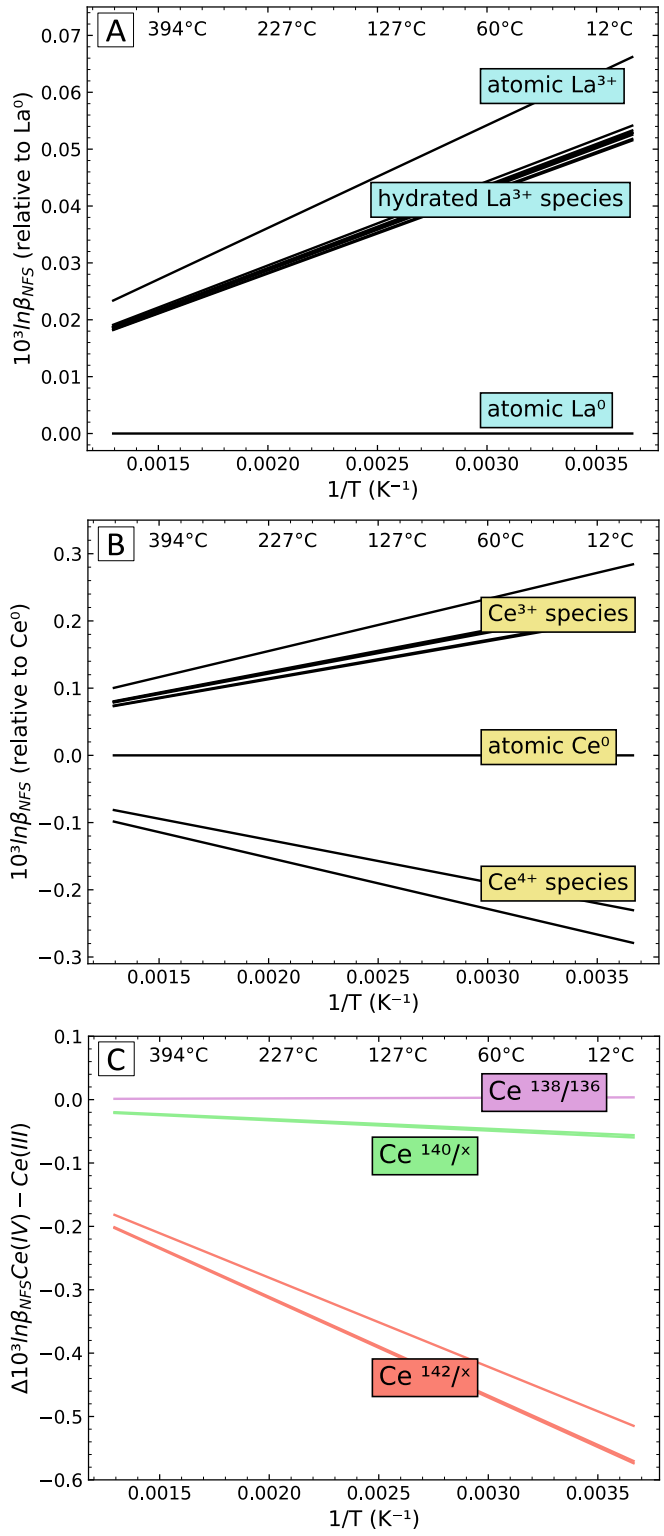

Fig. 5. Nuclear field shift effects as $10^3\ln\beta_{NFS}$ for (A) La-species, and (B) Ce-species. Values for La, and Ce are given relative to atomic La^0 and Ce^0, respectively. The $10^3\ln\beta$ values are grouped by their oxidation state indicating minimal isotope fractionation effects between species having identical oxidation states but significant fractionation when a change in oxidation state occurs. (C) $10^3\ln\beta_{NFS}$ values for the oxidation reaction of Ce^{3+} to Ce^{4+} for all possible Ce stable isotope ratios. Values are highly negative for $^{142}Ce/^{X}Ce$ due to the large difference in nuclear charge radius. By contrast, isotope fractionation between ^{140}Ce, ^{138}Ce, and ^{136}Ce is negligible due to their similar nuclear charge radii.

oxidation state but significantly when the oxidation state changes. The electron density at the nucleus follows the pattern: $REE^{2+}<REE^{3+}<REE^0$ in REE phases. Our calculated $10^3\ln\beta$ values show that trivalent La and Ce species are enriched in heavy isotopes relative to La^0 and Ce^0, respectively. This can be attributed to their lower $|\psi(0)|^2$ because of the missing 6s electrons in trivalent species. Through oxidation of Ce^{3+} to Ce^{4+}, a 4f electron is removed which decreases the shielding of the inner 5s electrons resulting in an increase in $|\psi(0)|^2$. This can explain the enrichment of lighter isotopes in Ce^{4+} over Ce^{3+}. Taken together, we are reasonably confident that the electronic structure calculations of the REE species presented herein are of good quality. The hydration of REE ions decreases $10^3\ln\beta_{NFS}$ indicating heavier isotopes in the non-hydrated species and therefore a slightly higher electron density at the nucleus in the hydrated REE species (Fig. 5A). We attribute this to the interaction of the negatively charged water oxygens with the positively charged REE nucleus which redistributes the electrons around the REE nucleus.

4.2. *Implications for REE mobility in high temperature hydrothermal systems*

Hydrothermal systems are dominated by elevated temperatures (100 ° – 500 °C), which reduces the magnitude of isotope fractionation observed since mass-dependent isotope fractionation is proportional to $1/T^2$ (Bigeleisen and Mayer, 1947; O'Neil, 1986). This temperature dependence makes it is more difficult to use REE element stable isotope systematics as tracers of the sources and the processes involved in the mobilisation and enrichment of REE. The maximum mass-dependent isotope fractionation between $NdCl_2$ and NdF for $\delta^{146/144}Nd$ decreases from 0.19 ‰ at 100 °C to only 0.053 ‰ at 500 °C (Fig. 2, Table 1), although at 500 °C this range of variability is still resolvable given the current achievable uncertainties on $\delta^{146/144}Nd = \pm 0.015$ ‰ (McCoy-West et al., 2020b). Therefore, $^{146}Nd/^{144}Nd$ can be a usable proxy to understand hydrothermal processes. For higher temperature systems (T > 500 °C), the analytical resolution would have to be increased or a different isotope pair with a larger relative mass difference needs to be utilised. Neodymium has a range of stable isotopes whose difference in nuclear charge radius increases relatively linearly with increasing mass difference (Fig. 7C). Thus, it can be expected that the proportion of NFS effects will remain constant for increasing mass differences of Nd isotopes. The use of $^{148}Nd/^{144}Nd$ for example, shows a maximum isotope fractionation range of 0.065 ‰ at 500 °C between NdF and $NdCl_2$ (Table S3). Similarly, the maximum isotope fractionation of Ce-species drops from 0.096 ‰ at 300 °C to 0.053 ‰ at 500 °C (Table 1) which comes below the current analytical uncertainty for $^{142}Ce/^{140}Ce$ (±0.04 ‰; Liu et al. (2023)). This limitation could also be overcome by utilising a greater relative mass differences such as $^{140}Ce/^{136}Ce$, if possible.

In hydrothermal systems, chloride, sulphate, and fluoride complexes are the main transporter of REE (Fig. 4A-C). The Thermoddem database is mostly based on the thermodynamic data from Haas et al. (1995) and therefore the proportion of hydroxide and fluoride species at elevated temperatures is overestimated, potentially by an order of magnitude (Migdisov et al., 2016). Fluoride is an important ligand for REE mobilisation in hydrothermal fluids and its destabilisation contributes to bastnäsite ($REEFCO_3$) formation, the most abundant REE-mineral in hydrothermal systems (Migdisov and Williams-Jones, 2014). Since Fluoride complexes are isotopically heavy, their destabilisation would create a pool of heavy REE isotopes that form the source of REE incorporated into minerals (e.g. bastnäsite). Fluoride bearing REE minerals can therefore be expected to be heavier than the bulk composition of the hydrothermal fluid. It can also be inferred from the aqueous complexes that bonds with fluoride in the crystal lattice like in bastnäsite will incorporate heavier isotopes from the fluid owing to the high electronegativity of fluorine.

Additional complications could arise when REE ion coordination number changes. It has been demonstrated in molecular dynamics and X-ray absorption spectroscopy studies that the coordination number of

Table 2
Calculated $10^3 \ln\beta_{NFS}$ (NFS = Nuclear Field Shift) values for aqueous La, and Ce complexes. Values are given relative to La^0 and Ce^0, respectively.

Species	Temperature (°C)							
	0	25	50	100	200	300	400	500
Lanthanum Species								
La^{3+}	0.066	0.061	0.056	0.048	0.038	0.032	0.027	0.023
$La(H_2O)_9^{3+}$	0.053	0.049	0.045	0.039	0.031	0.025	0.022	0.019
$La(H_2O)_8^{3+}$	0.051	0.047	0.043	0.037	0.030	0.024	0.021	0.018
$LaCl(H_2O)_8^{2+}$	0.053	0.048	0.045	0.039	0.031	0.025	0.021	0.019
$LaCl(H_2O)_7^{2+}$	0.051	0.047	0.038	0.043	0.030	0.024	0.021	0.018
$LaF(H_2O)_8^{2+}$	0.053	0.048	0.045	0.039	0.031	0.025	0.021	0.019
$LaSO_4(H_2O)_7^{+}$	0.054	0.050	0.046	0.040	0.031	0.026	0.022	0.019
$LaCO_3(H_2O)_8^{+}$	0.052	0.047	0.044	0.038	0.030	0.025	0.021	0.018
$LaHCO_3(H_2O)_7^{2+}$	0.053	0.048	0.044	0.038	0.030	0.025	0.021	0.019
$LaOH(H_2O)_8^{2+}$	0.053	0.048	0.045	0.039	0.030	0.025	0.021	0.019
$LaHS(H_2O)_8^{2+}$	0.052	0.047	0.044	0.038	0.030	0.025	0.021	0.018
Cerium Species								
Ce^{3+}	0.284	0.260	0.240	0.208	0.164	0.135	0.115	0.100
Ce^{4+}	−0.230	−0.211	−0.195	−0.169	−0.133	−0.110	−0.093	−0.081
$Ce(H_2O)_9^{3+}$	0.207	0.190	0.175	0.152	0.120	0.099	0.084	0.073
$Ce(H_2O)_9^{4+}$	−0.279	−0.256	−0.236	−0.204	−0.161	−0.133	−0.113	−0.099
$Ce(H_2O)_8^{3+}$	0.216	0.198	0.182	0.158	0.124	0.103	0.087	0.076
$CeCl(H_2O)_8^{2+}$	0.226	0.207	0.191	0.165	0.130	0.107	0.092	0.080
$CeF(H_2O)_8^{2+}$	0.210	0.192	0.177	0.153	0.121	0.100	0.085	0.074
$CeCO_3(H_2O)_8^{+}$	0.223	0.204	0.188	0.163	0.129	0.106	0.090	0.079
$CeHCO_3(H_2O)_7^{2+}$	0.225	0.206	0.191	0.165	0.130	0.107	0.091	0.080
$CeOH(H_2O)_8^{2+}$	0.228	0.209	0.193	0.167	0.132	0.109	0.092	0.080

Table 3
Overview of computational setups used for hydrated La^{3+} to find good agreement with experimental data of vibrational frequencies. Various basis sets and a combination of explicit and implicit solvation effects were used. Two explicit hydration shells in combination with implicit solvation effects using a continuum model (CPCM) shows best agreement with the experimental value of 343 cm^{-1} for the La-O stretch (Rudolph and Irmer, 2020). The PBE0 functional was used for all calculations.

Species	CPCM	La basis set	H, O basis set	ECP	ν_1La-O (cm^{-1})
$La(H_2O)_9^{3+}$	no	def2-tzvp	def2-tzvp	SD	281
$La(H_2O)_9^{3+}$	yes	def2-tzvp	def2-tzvp	SD	308
$La(H_2O)_9^{3+}$	yes	def2-svp	def2-svp	SD	318
$La(H_2O)_9^{3+}$	yes	LANL2TZ	6-31G(d,p)	Hay-Wadt	312
$La(H_2O)_9^{3+}$	yes	def2-tzvp	def2-svp	SD	318
$La(H_2O)_9(H_2O)_{14}^{3+}$	no	def2-tzvp	def2-svp	SD	334
$La(H_2O)_9(H_2O)_{16}^{3+}$	yes	def2-svp	def2-svp	SD	338
$La(H_2O)_9(H_2O)_{16}^{3+}$	yes	def2-tzvp	def2-svp	SD	344

La, and Nd complexes in a chloride solution gradually decreases with increasing temperature (e.g. from CN = 8.2 at 200 °C to CN = 5.9 at 500 °C) along with a change in average number of inner sphere Cl^--ions (e.g. n = 1 at 200 °C to n = 3.4 at 500 °C) (Brugger et al., 2016; Guan et al., 2022; Mayanovic et al., 2009). For this purpose, some high-temperature species of REE with a lower coordination number have been modelled, namely $REE(H_2O)_8$ and $REECl(H_2O)_7$, in order to estimate how isotope fractionation will change at elevated temperature due to the reduction of the REE coordination number. We calculated the isotope fractionation for the ligand exchange reaction (H_2O molecules are omitted for simplicity):

$$REE^{3+} + REE'Cl^{2+} = REE'^{3+} + REECl^{2+} \quad (9)$$

at 200 °C and compared them with their lower temperature counterparts $REE(H_2O)_9$ and $REECl(H_2O)_8$, respectively (Fig. 9). The β-factors of the individual high-temperature species are higher because of their lower coordination number which allows the surrounding atoms and molecules to move closer to the REE ion which leads to shorter and stronger bonds that favour heavier isotopes. However, the increase in $10^3 \ln\beta$ is not identical for all species and the magnitude of isotope fractionation can be diminished or even inversed compared to lower temperature coordination environment. As shown for La (Fig. 9A) changing the coordination can also invert the NFS effect, however, its contribution to the total fractionation is still negligible if no change in oxidation state occurs. Therefore, due to these complexities simplified modelling of temperature dependent isotope fractionation in aqueous solutions at elevated temperatures should be treated with caution.

Similar to aqueous complexes, correlations of β-factors with coordination number and bond lengths have been identified in solid phases using DFT (Ducher et al., 2016; Schauble, 2011). For example, Nd has a coordination number of 9 in idealized Nd-monazite with average Nd-O of 2.57 Å (Ni et al., 1995) which lies in the range of bond length values for Nd-complexes obtained in this study (2.46 – 2.55 Å; Table S6). This implies equilibrium fractionation between hydrothermal fluids and minerals can also exceed analytical uncertainties at elevated temperature (>500 °C). However, β-factors for different minerals are required to properly understand isotope fractionation between fluids and precipitates which is beyond the scope of this study.

Furthermore, fluid mixing at hydrothermal vents induces rapid mineral precipitation meaning isotopic fractionation is dominated by kinetic isotope effects (McCoy-West et al., 2020a) which concentrates lighter isotopes in the hydrothermal minerals that prevents them from re-equilibration with the ambient fluid (Wilkinson et al., 2005). Therefore, β-factors do not provide very reliable information on disequilibrium processes that are common at hydrothermal vents. Overall, various difficulties might arise in high temperature systems such as fluid mixing, decreasing magnitude of isotope fractionation, and changes in coordination numbers that complicate the application of theoretical calculations of isotope fractionation in such systems.

4.3. Implications for REE mobility in low-temperature systems and resource exploration

Clay-hosted REE deposits have become of increasing commercial and scientific interest in recent years (Jowitt et al., 2017; Sanematsu et al., 2016). Isotopes could serve as potential tracer to improve our understanding of the interplay of source rock weathering and enrichment processes that form these deposits. Clay-hosted deposits form in low temperature groundwater (T < 30 °C) where isotope fractionation will not be significantly diminished by the temperature effect. Weathering of

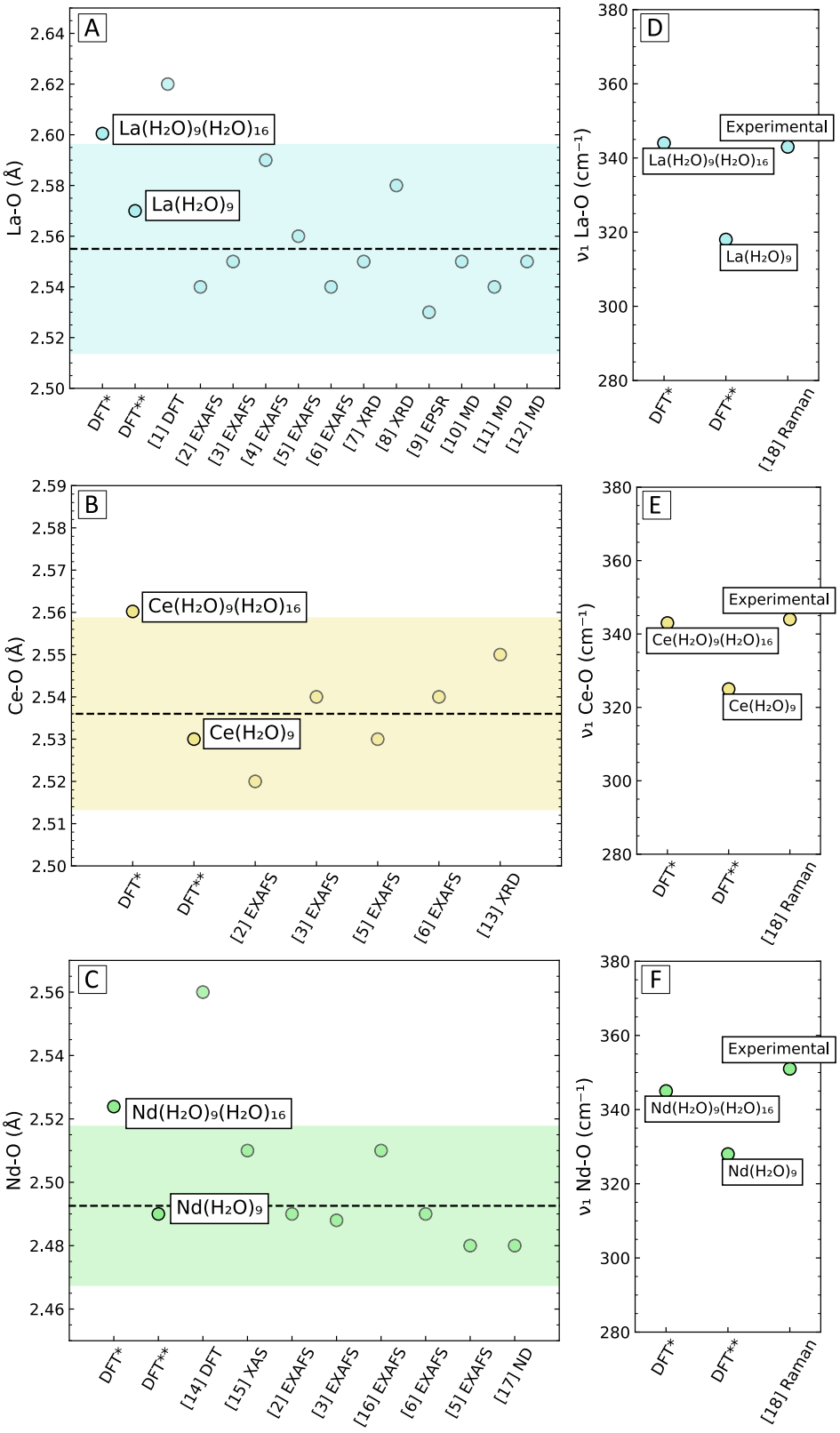

(caption on next page)

Fig. 6. Comparison of REE-O bond lengths (A-C) and vibrational frequencies of the symmetric REE-O stretch (D-F) in hydrated REE^{3+} (REE = La, Ce, Nd). Data derived from a range of computational and experimental methods. Bond lengths from DFT calculations herein utilising one hydration shell and implicit solvation effects (**) show an excellent agreement with experimental data by plotting within the 2 standard deviation interval (highlighted area) of average experimental data (dashed line; DFT and MD studies excluded) while calculations using two hydration shells plus implicit solvation effects (*) plot outside. Computations using two hydration shells (**) show very good agreement with experimental vibrational frequencies. References: [1] Clark (2008), [2] Allen et al. (2000), [3] Ishiguro et al. (2002), [4] Anderson et al. (2002), [5] Solera et al. (1995), [6] Persson et al. (2008), [7] Grigoriew and Siekierski (2002), [8] Habenschuss and Spedding (1979), [9] Diaz-Moreno et al. (2011), [10] Petit et al. (2008), [11] Beuchat et al. (2010), [12] Guan et al. (2022), [13] Johansson (1992), [14] Cosentino et al. (2000), [15] Mayanovic et al. (2009), [16] Yamaguchi et al. (1988), [17] Narten and Hahn (2002), [18] Rudolph and Irmer (2020). Abbreviations: DFT = Density Functional Theory, EXAFS = Extended X-ray Absorption Fine Structure, XRD = X-ray diffraction, EPSR = Empirical Structure Refinement, MD = Molecular Dynamics, XAS = X-ray Absorption Spectroscopy, ND = Neutron Diffraction.

host minerals such as monazite, apatite and xenotime determine the isotopic composition of the source fluid but pedogenic processes like complexation, availability of ligands and adsorption control the enrichment of REE in economically relevant concentrations (Jowitt et al., 2017).

In contrast to divalent base metals such as Ni, Zn, or Cu, most anion-complexes of trivalent lanthanides (e.g. $REESO_4^+$ or $REECO_3^+$) retain their positive charge which makes them potential adsorbates on negatively charged surfaces (Yang et al., 2019). The surface charge of sediment particles is mainly controlled by pH and is generally negative around circumneutral pH (Stumm and Morgan, 1995) which is a relevant pH spectrum for the deeper part of clay-hosted REE deposits (Borst et al., 2020; Liang et al., 2024). Isotope fractionation between different possible adsorbed surface complexes is poorly understood, but our data strongly supports the idea that variations in the bonding environments of REE in surface complexes will cause isotope fractionation comparable to that observed in aqueous complexes, although some insights are available. Bai et al. (2023) demonstrated that in a basaltic weathering profile REE adsorption onto gibbsite and Fe-oxides can generate resolvable Nd isotope fractionations of $\delta^{146/144}$Nd up to 0.21 ‰. This is comparable to the range of observed variations in $\delta^{142/140}$Ce of 0.3 ‰ seen in bauxites (Li et al., 2023a). Theoretically the formation of 8–9 ninefold coordinated REE as outer-sphere surface complexes on kaolinite (Borst et al., 2020) would predict limited isotope fractionation between adsorbed and dissolved species should occur due to the invariant coordination number. However, the maximum difference in Nd isotopic composition among 9-fold Nd aqueous species from Fig. 3C, F presented herein is $\Delta 10^3 ln\beta_{NdF\text{-}Nd} = 0.22$. This value agrees very well with the magnitude of the isotope fractionation observed in the Bai, J. et al. (2023) study (0.21 ‰). Isotope fractionation in weathering profiles can, therefore, potentially be explained through preferential adsorption of a specific ligand-bearing aqueous complexes to 9-fold outer-sphere complexes. For example, Li et al. (2022) suggest that carbonate complexes are preferentially adsorbed on clay minerals which makes their isotopic composition heavier than the original REE^{3+} bearing source fluid. Adsorption experiments have shown that the availability of carbonate ligands can change isotope fractionation during adsorption for Ce (Nakada et al., 2017). In groundwater due to the pH (<10), REE are predominantly speciated as free REE^{3+} or (bi-)carbonate complexes. However, modelling by Tang and Johannesson (2010) has shown that REE are mostly adsorbed as free REE^{3+} from a pool of lighter adsorbed species while the heavier isotopes are kept in solution as carbonate complexes. An additional complication is carbonate complexation is pH dependent as is the adsorption capability of mineral particles. This leads to a smaller proportion of isotopically lighter free REE^{3+} available at higher pH (> 6) for adsorption (Fig. 3). Neodymium-carbonate complexes can only be up to 0.11 ‰ heavier than free Nd^{3+} at 25 °C which is significantly smaller than the range of isotopic composition currently observed in weathering profiles ($\delta^{146/144}$Nd = 0.21 ‰; Bai et al., 2023). Further isotope fractionation of sorbed carbonate complexes can be expected through changes in coordination number and bond lengths during adsorption. As demonstrated by Nakada et al. (2013b), light REE exhibit a lower coordination number for La, Ce, and Nd on ferrihydrite and Mn-oxides than in aqueous solution. Therefore, an even larger fractionation between adsorbed and aqueous REE than between aqueous complexes can be expected. We conclude that even the formation of 9-fold outer-sphere complexes can cause significant isotope fractionation between fluids and clay minerals, but it is not sufficient to explain the entire range of isotopic variation observed in the so far limited previous studies. We predict even larger fractionations can be expected associated with other mineral phases where greater changes in coordination number and bond lengths occur.

4.4. Implications from nuclear field shift (NFS) effects for interpretation of Ce isotope data

Most REE only exist as trivalent cations in terrestrial environments except for Ce and Eu. Oxidation causes larger isotope fractionations than changes in atomic coordination which makes Ce isotope signatures an interesting potential proxy for oxidation. Negative and positive Ce anomalies (Ce enriched or depleted relative to other REE) are a common occurrence in weathering profiles and marine sediments (Berger et al., 2014; Borst et al., 2020). However, Ce anomalies in marine sediments like banded iron formations can occur regardless of their formation age relative to the great oxidation event (Kato et al., 2006), and this has been attributed to fluid overprints during later diagenesis (Basu et al., 2022; Bonnand et al., 2020). Stable Cerium isotopes are potentially a sensitive proxy for anoxic to suboxic and oxic conditions (Nakada et al., 2016) and a few pilot studies on Ce isotope signatures have been published recently (Bai et al., 2024; Bonnand et al., 2023; Li et al., 2023a; Li et al., 2023b; Nakada et al., 2016; Nakada et al., 2017; Pourkhorsandi et al., 2021). Cerium is removed from seawater by oxidation to the insoluble Ce^{4+} in modern environments through oxidative adsorption or precipitation as cerianite (CeO_2) and ceric hydroxide ($Ce(OH)_4$).

The β-factors of Ce^{4+} derived herein (Fig. 2B, Table 1) show that there is a preference for heavier isotopes in the higher oxidation state from a mass dependent perspective in accordance with the theoretical principles of mass-dependent isotope fractionation (Schauble, 2004). Our results from first principles calculations provide evidence that mass-dependent isotope fractionation between hydrated Ce^{3+} and Ce^{4+} is significant ($\Delta 10^3 ln\beta_{Ce(IV)\text{-}Ce(III)} = 0.46$ at 25 °C) and should be measurable when NFS effects are neglected. However, previous laboratory experiments have shown the inverse behaviour of Ce during adsorption and precipitation in aqueous systems. It has been demonstrated that Ce in Ce^{4+}-oxides and surface complexes favours lighter isotopes although its bonding environment shows shorter bonds, lower coordination number and a higher oxidation state than the Ce^{3+} in solution (Bonnand et al., 2023; Nakada et al., 2013a; Nakada et al., 2017). Each of those parameters is predicted to be associated with the incorporation of heavier isotopes as they make stronger bonds. In the aforementioned experiments, the $^{142}Ce/^{140}Ce$ isotope ratio was used and the preferred incorporation of lighter isotopes in Ce^{4+} was suggested to be the result of distorted surface complexes or NFS effects. Our results demonstrate that the $^{142}Ce/^{140}Ce$ ratio is heavily affected by NFS effects with the preference for lighter isotopes occurring in the higher oxidation state (i.e. Ce^{4+}) for $^{142}Ce/^{140}Ce$ signatures (Fig. 5C), thus NFS effects might explain the previous unexpected experimental observations. However, debate remains as to whether oxidative Ce adsorption occurs on ferrihydrite (Bau and Koschinsky, 2009; Nakada et al., 2013a). Assuming no oxidative adsorption occurs, even considering NFS effects, we cannot

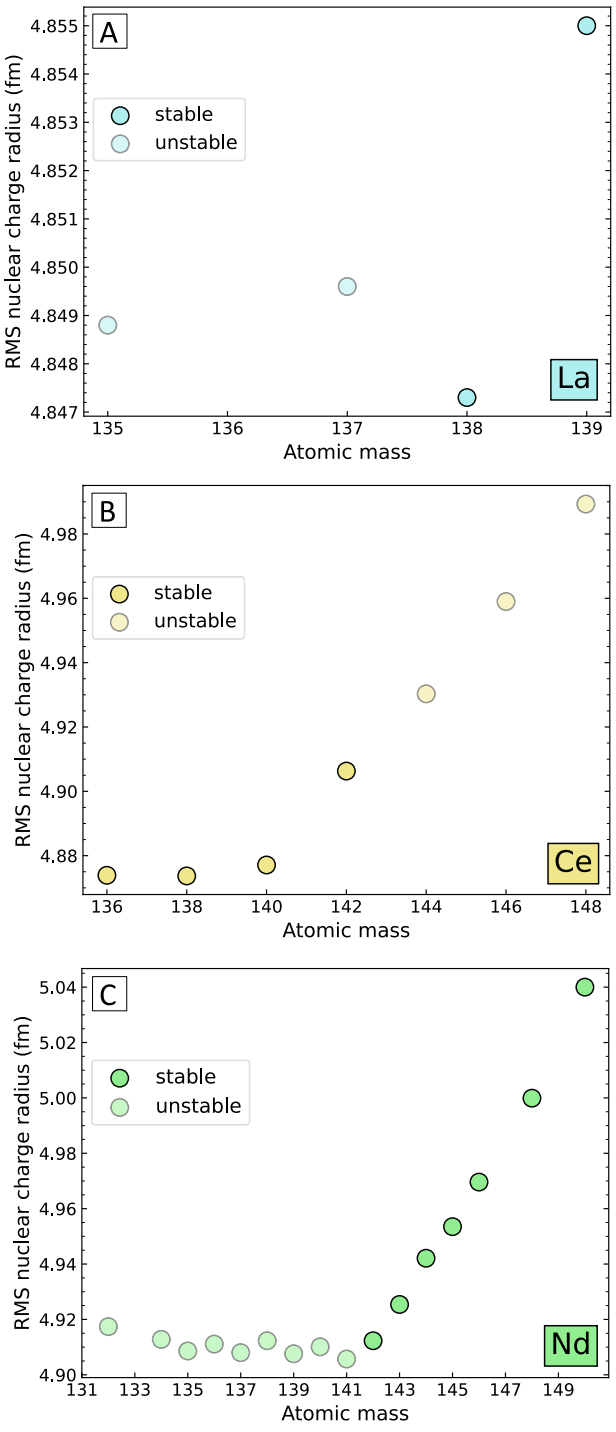

Fig. 7. Root mean square (RMS) nuclear charge radii versus atomic mass for (A) La, (B) Ce, and (C) Nd isotopes. Lanthanum has only two stable isotopes with a mass difference of 1 amu which makes measurements of isotope fractionation very inflexible. The lightest Ce isotopes (^{136}Ce, ^{138}Ce, and ^{140}Ce) have very similar nuclear charge radii making it possible to minimise NFS effects. By contrast, Nd isotopes with similar nuclear charge radii are unstable. Data from Angeli and Marinova (2013).

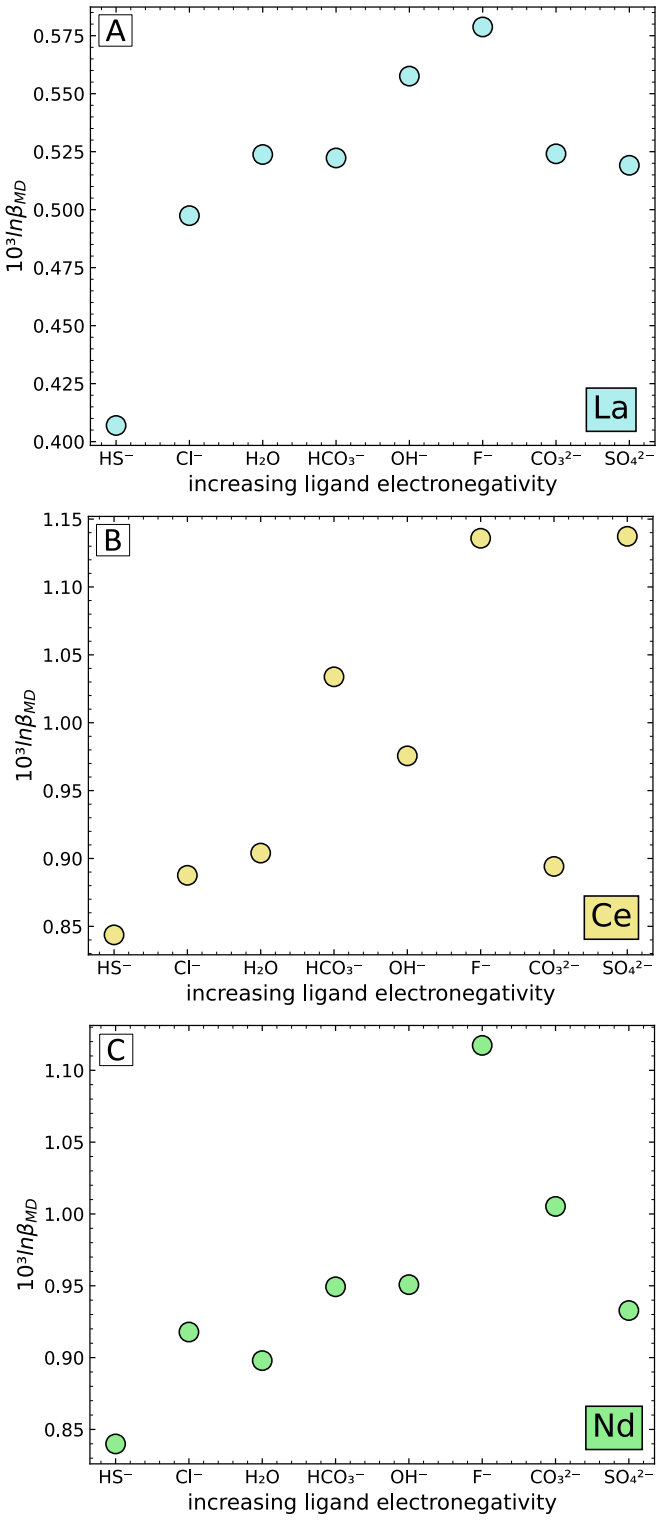

Fig. 8.C. Calculated $10^3 \ln\beta_{MD}$ at 25 °C versus ligand electronegativity shows a general trend towards heavier REE isotopes favouring bonding partner with higher electronegativity. The larger the difference in electronegativity between REE and the ligand, the stronger the bond which is favoured by heavier isotopes. Order of electronegativity adapted from Fujii et al. (2014) with value for fluorine from Allred (1961).

explain why lighter isotopes would adsorb on ferrihydrite but also that the bond length and coordination number of adsorbed Ce is smaller than in aqueous complexes as shown in Nakada et al. (2013b) and Nakada et al. (2017) since we would not expect significant NFS effects without a change in oxidation state for Ce. Conversely, assuming oxidative adsorption of Ce by ferrihydrite does occur (e.g. as observed by Bau and Koschinsky (2009)) NFS effects may help explain the anomalous experimental results. Namely, the $10^3 ln\beta$ for the NFS for Ce oxidation ($10^3 ln\beta_{Ce(IV)\text{-}Ce(III)} = -0.45$ at 25 °C). However, this value deviates only slightly from the mass dependent difference between hydrated Ce^{3+} and

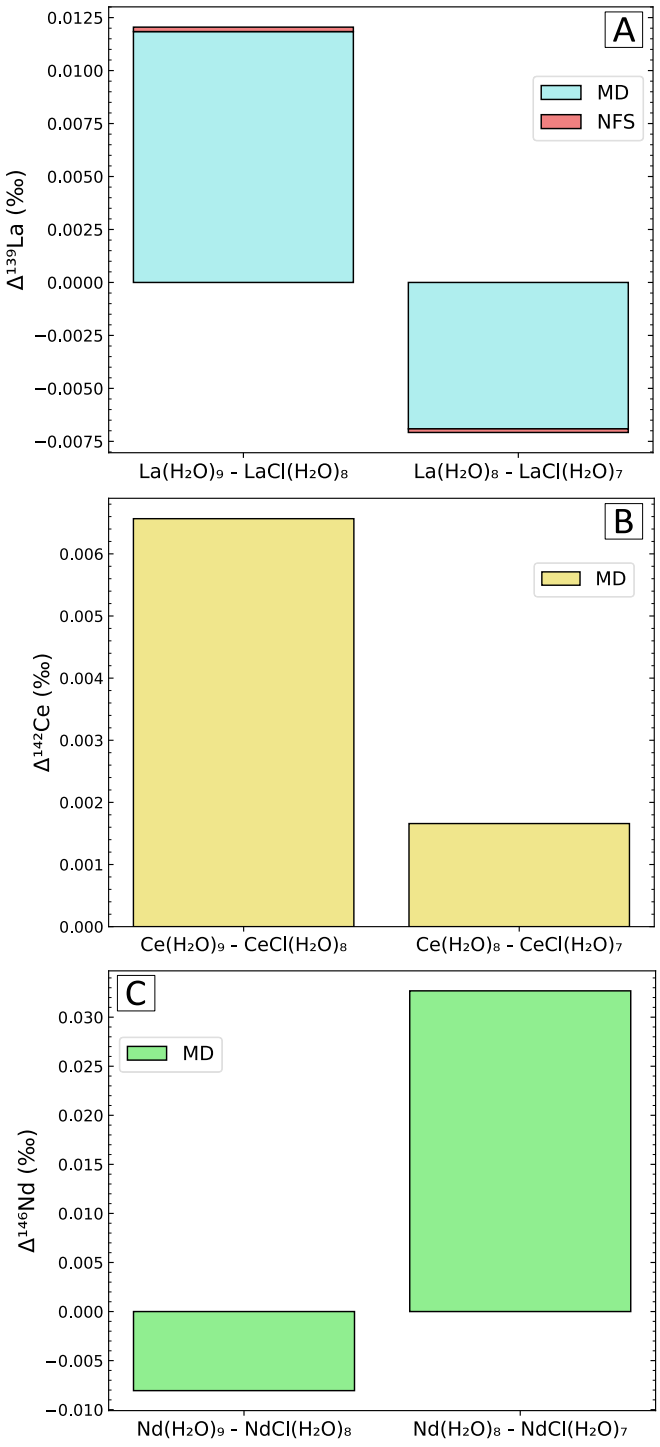

Fig. 9. Isotope fractionation of the ligand exchange reaction between free hydrated REE^{3+} and REECl at 200 °C using two different REE coordination numbers for the same complexes is illustrated here for (A) La, (B) Ce, and (C) Nd complexes. Where for example $\Delta^{146}Nd$ is $10^3(\ln\beta_{Nd} - \ln\beta_{NdCl})$. Bar plots on the left represent higher coordination number (i.e. REE coordination expected at lower temperatures) while the bar plots on the right have a lower coordination number (i.e. REE coordination expected at higher temperatures). As the coordination number of aqueous metal complexes decreases with increasing temperature, the isotope fractionation between aqueous complexes can potentially diminish or become inversed compared to the species observed at room temperature.

Ce^{4+} ($10^3 ln\beta_{Ce(IV)\text{-}Ce(III)} = +0.46$ at 25 °C). This competing combination of effects strongly suggests that minimal net isotope fractionation occurs during Ce oxidation around room temperature meaning $^{142}Ce/^{140}Ce$ signatures are not an ideal tracer of oxidation (Fig. 10). This result is in agreement with Schauble (2023) who found a near cancelation of mass-dependent effects by the NFS effect for $^{142}Ce/^{140}Ce$ isotope fractionation between Ce^{4+}-oxide and Ce^{3+}-monazite. Additionally, a recent study looking at Ce isotopes in diamictites sampled across the Great Oxidation Event (GOE) shows no change in the isotopic composition of Ce although a clear change in oxidation state of Ce occurs post-GOE (Li et al., 2023b). Nonetheless, Bonnand et al. (2023) continues to argue that $^{142}Ce/^{140}Ce$ is a potential redox proxy with lighter isotopes concentrated in the oxidised phases.

Cerium has four stable isotopes, with the three lightest isotopes ^{136}Ce, ^{138}Ce, and ^{140}Ce having extremely similar nuclear charge radii (~4.874 – 4.877 fm), whereas the heavier isotope ^{142}Ce (4.907 fm) has a distinctly different nuclear charge radius (Fig. 7B). Our theoretical calculations show that the similar nuclear charge radii of ^{136}Ce, ^{138}Ce, and ^{140}Ce produce a negligible NFS effect during Ce^{3+} oxidation (−0.06 to 0.003 at 25 °C; Fig. 5C) which would improve the ability to use Ce isotope signatures as a proxy for changes in oxidation states. Due to the greatly higher natural abundance of the isotopes (at least 44 times), measurement of the $^{142}Ce/^{140}Ce$ isotope ratio has been favoured, although if the analytical challenges could be overcome it would be worthwhile considering using other isotope pairs for future studies to eliminate the substantial influence from NFS effects on Ce isotopes.

The NFS effect is proportional to 1/T while mass-dependent isotope fractionation is proportional to $1/T^2$. This means NFS effects contribute a higher proportion of isotope fractionation in high temperature hydrous environments like hydrothermal systems (200 ° – 500 °C). Table 4 shows that, for example, the proportion of isotope fractionation associated with NFS reaches only 4.5 % of total isotope fractionation at 500 °C for the sulphate-sulphide redox reaction (H_2O molecules are omitted for simplicity):

$$LaHS^- + 2O_2 = LaSO_4^{2-} + H^+ \quad (10)$$

Consequently, NFS effects can be considered to remain relatively small, and are thus insignificant for hydrous systems unless changes in oxidation state occur. Oxidation of a reduced fluid can significantly fractionate the isotopic composition of aqueous complexes enriching the

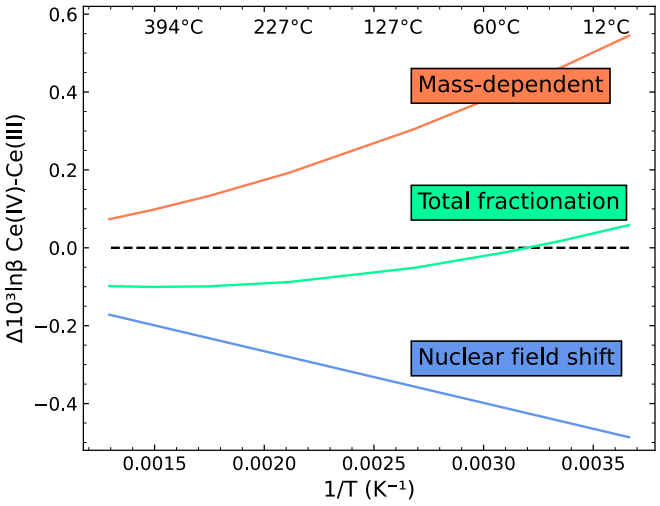

Fig. 10. Mass-dependent (MD) and nuclear field shift (NFS) effects for the oxidation reaction of hydrated Ce^{3+} to Ce^{4+}. The MD fractionation is nearly cancelled at room temperature and inversed at elevated temperatures, which leads to an incorporation of lighter isotopes in the higher oxidation state. This raises the question whether the $^{142}Ce/^{140}Ce$ isotope ratio is a useful proxy for oxidation in future studies.

Table 4
Mass-dependent (MD) and nuclear field shift (NFS) effect in $\Delta 10^3 \ln\beta$ for the sulphide-sulphate redox reaction $LaHS^- + 2O_2 = LaSO_4^{2-} + H^+$. With increasing temperature, the proportion of NFS increases because of its proportionality to $1/T$ whereas MD is proportional to $1/T^2$. However, even at temperatures of 500 °C, the proportion of NFS on the total isotope fractionation remains below 5 %. Mass-independent NFS effects are negligible for REE as long as no change in oxidation state occurs which is the case for most REE in terrestrial environments.

T (°C)	MD	NFS	%NFS
0	−0.1323	−0.0023	1.74
25	−0.1122	−0.0021	1.87
50	−0.0963	−0.0020	2.01
100	−0.0731	−0.0017	2.29
200	−0.0462	−0.0013	2.84
300	−0.0317	−0.0011	3.39
400	−0.0231	−0.0009	3.94
500	−0.0176	−0.0008	4.48

S-bearing -complexes with heavier isotopes by 0.1 ‰ at 25 °C (Table 1). Ultimately, therefore theoretical predictions for mass-dependent isotope fractionation still provide extremely valuable information on the magnitude and direction of isotope fractionation in high temperature aqueous systems, however, when a change in oxidation state occurs caution should be exercised.

5. Summary

Using a combination of aqueous speciation modelling and theoretical calculations the isotope fractionation between aqueous complexes of La, Ce and Nd have been investigated.

(1) This work provides a comprehensive dataset of reduced partition function ratios ($10^3 ln\beta$) of light REE applicable to hydrous systems. This knowledge provides a foundation to enable the application of REE stable isotope measurements to a range of areas of geoscience in the future.
(2) To obtain accurate vibrational frequencies in aqueous REE complexes, the presence of a second explicit hydration shell was required in addition to implicit solvation effects. However, REE-O bond lengths within the first hydration shell are more accurately described when only using one explicit hydration shell together with implicit solvation effects.
(3) Prediction of isotope fractionation from $10^3 ln\beta$ values can be difficult in high temperature systems or where kinetic isotope effects occur. The general decrease of isotope fractionation with rising temperature can prevent isotope fractionation being measured, especially for heavy elements like REE. The increasing proportion of NFS effects on the total fractionation with increasing temperature does not mask the mass-dependent fractionation to a noticeable extent if no change in oxidation state of the REE occurs. However, as the coordination number changes with increasing temperature, the isotope fractionation can be diminished or even inversed compared to predictions made from species with higher coordination numbers.
(4) This dataset will be of particularly interest for understanding ion adsorption deposits because of the elevated isotope fractionation at low fluid temperatures and their enrichment through adsorption where surface complexes are in exchange equilibrium with the source fluid. Depending on the sorbed species, modelling herein shows that the proportion and isotopic composition of aqueous complexes available for sorption varies with fluid conditions.
(5) Previous Ce isotope adsorption experiments for Ce produced results contrary to predictions based on isotope theory and have been related to NFS effects. The magnitude of NFS for $^{142}Ce/^{140}Ce$ is significant ($10^3 ln\beta_{Ce(IV)\text{-}Ce(III)} = -0.45$ at 25 °C) and nearly cancels mass-dependent isotope fractionation during oxidation ($10^3 ln\beta_{Ce(IV)\text{-}Ce(III)} = +0.46$ at 25 °C) which means the $^{142}Ce/^{140}Ce$ isotope ratio is not a suitable proxy for oxidation. If possible, the use of other Ce isotope pairs with more similar nuclear charge radii can greatly reduce NFS effects. The large mass-dependent isotope fractionation effect of Ce^{3+} oxidation ($10^3 ln\beta_{Ce(IV)\text{-}Ce(III)} = +0.46$ at 25 °C) is considered a promising indicator that Ce could be a usable tracer for oxidation if NFS effects are minimized.

CRediT authorship contribution statement

Mark Nestmeyer: Writing – original draft, Visualization, Validation, Methodology, Investigation, Formal analysis, Data curation, Conceptualization. **Alex J. McCoy-West:** Writing – original draft, Validation, Supervision, Project administration, Investigation, Funding acquisition, Conceptualization.

Data availability

Data are available through Research Data JCU at https://doi.org/10.25903/2ky5-yh72.

Declaration of competing interest

The authors declare that they have no known competing financial interests or personal relationships that could have appeared to influence the work reported in this paper.

Acknowledgments

This study has been supported by High Performance Computer resources at James Cook University and Pawsey Supercomputing Research Centre. MN thanks JCU for a Postgraduate Research Stipend Scholarship. We thank Avish Kumar and Brandon Mahan for discussions. This project was supported by ARC grant DE210101395 to AMW. We thank three anonymous reviews and the editor for comments that improved the clarity of the computational setup.

Appendix A. Supplementary material

The supplementary material contains various additional figures and tables. Fig. S1 illustrates geometric isomers of chloride-, fluoride-, and hydroxide-complexes of Lanthanum. Fig. S2 shows the mass-dependent isotope fractionation between geometric isomers of La. Fig. S3 presents relativistic and non-relativistic total energy calculations of (A) La^0 and (B) Ce^0 using Dirac-Hartree-Fock with different basis sets and Hamiltonians. Energies are compared with results from previously published values. Fig. S4 shows $10^3 \ln\beta_{NFS}$ for La^{3+} relative to La^0 derived from various relativistic and non-relativistic calculations using different basis sets. Table S1 contains the fluid parameters used for the PHREEQC simulations. Table S2 shows the electron configuration for atomic and ionic La and Ce used for nuclear field shift calculations. Table S3 presents $10^3 \ln\beta_{MD}$ values of $^{148}Nd/^{144}Nd$ aqueous complexes. Table S4 contains $10^3 \ln\beta_{NFS}$ values for the oxidation of Ce^{3+} to Ce^{4+} for all possible ratios for stable Ce isotopes. Table S5 compares computed vibrational frequencies in the REE-O stretch with experimental data. Table S6 gives an overview of REE-O bond lengths derived from theoretical calculations and experimental studies. Table S7 compares ionisation energies for La and Ce calculated in this study with experimental data. Supplementary material to this article can be found online at https://doi.org/10.1016/j.gca.2024.10.007.

References

Abe, M., Suzuki, T., Fujii, Y., Hada, M., 2008. An ab initio study based on a finite nucleus model for isotope fractionation in the U(III)-U(IV) exchange reaction system. J. Chem. Phys. 128 (14), 144309.

Adamo, C., Barone, V., 1999. Toward reliable density functional methods without adjustable parameters: The PBE0 model. J. Chem. Phys. 110 (13), 6158–6170.

Albarède, F., Télouk, P., Balter, V., 2017. Medical applications of isotope metallomics. Rev. Mineral. Geochem. 82 (1), 851–885.

Allen, P.G., Bucher, J.J., Shuh, D.K., Edelstein, N.M., Craig, I., 2000. Coordination chemistry of trivalent lanthanide and actinide ions in dilute and concentrated chloride solutions. Inorg. Chem. 39 (3), 595–601.

Allred, A.L., 1961. Electronegativity values from thermochemical data. J. Inorg. Nucl. Chem. 17 (3–4), 215–221.

Anderson, A.J., Jayanetti, S., Mayanovic, R.A., Bassett, W.A., Chou, I.M., 2002. X-ray spectroscopic investigations of fluids in the hydrothermal diamond anvil cell: The hydration structure of aqueous La^{3+} up to 300 °C and 1600 bars. Am. Mineral. 87 (2–3), 262–278.

Angeli, I., Marinova, K.P., 2013. Table of experimental nuclear ground state charge radii: An update. At. Data Nucl. Data Tables 99 (1), 69–95.

Bai, J.-H., Lin, M., Zhong, S.-X., Deng, Y.-N., Zhang, L., Luo, K., Wu, H., Ma, J.-L., Wei, G.-J., 2023a. High intermediate precision Sm isotope measurements in geological samples by MC-ICP-MS. J. Anal. At. Spectrom 38 (3), 629–637.

Bai, J., Luo, K., Wu, C., Wang, Z., Zhang, L., Yan, S., Zhong, S., Ma, J., Wei, G., 2023b. Stable neodymium isotopic fractionation during chemical weathering. Earth and Planetary Science Letters 617.

Bai, J., Wu, C., Wu, H., Wang, Z., Zhang, L., Zhong, S., Ma, J., Wei, G., 2024. δ^{142}Ce minus δ^{146}Nd value as a redox indicator in Earth's surface environments. Earth and Planetary Science Letters 629.

Basu, P., Ishwar-Kumar, C., Chaudhary, S., Chakrabarti, R., Satish-Kumar, M., Sajeev, K., 2022. Major, trace element, and Nd isotopic compositions of banded iron formation and shales from the Sirsi shelf, Dharwar Craton, India: Implications for paleo-seawater chemistry, post-depositional alteration, and provenance. Precambr. Res. 382.

Bau, M., Koschinsky, A., 2009. Oxidative scavenging of cerium on hydrous Fe oxide: Evidence from the distribution of rare earth elements and yttrium between Fe oxides and Mn oxides in hydrogenetic ferromanganese crusts. Geochem. J. 43 (1), 37–47.

Berger, A., Janots, E., Gnos, E., Frei, R., Bernier, F., 2014. Rare earth element mineralogy and geochemistry in a laterite profile from Madagascar. Appl. Geochem. 41, 218–228.

Beuchat, C., Hagberg, D., Spezia, R., Gagliardi, L., 2010. Hydration of lanthanide chloride salts: a quantum chemical and classical molecular dynamics simulation study. J. Phys. Chem. B 114 (47), 15590–15597.

Bigeleisen, J., 1998. Second-order correction to the Bigeleisen-Mayer equation due to the nuclear field shift. PNAS 95 (9), 4808–4809.

Bigeleisen, J., Mayer, M.G., 1947. Calculation of equilibrium constants for isotopic exchange reactions. J. Chem. Phys. 15 (5), 261–267.

Black, J.R., Kavner, A., Schauble, E.A., 2011. Calculation of equilibrium stable isotope partition function ratios for aqueous zinc complexes and metallic zinc. Geochim. Cosmochim. Acta 75 (3), 769–783.

Blanc, P., Lassin, A., Piantone, P., Azaroual, M., Jacquemet, N., Fabbri, A., Gaucher, E.C., 2012. Thermoddem: A geochemical database focused on low temperature water/rock interactions and waste materials. Appl. Geochem. 27 (10), 2107–2116.

Bonnand, P., Lalonde, S.V., Boyet, M., Heubeck, C., Homann, M., Nonnotte, P., Foster, I., Konhauser, K.O., Köhler, I., 2020. Post-depositional REE mobility in a Paleoarchean banded iron formation revealed by La-Ce geochronology: A cautionary tale for signals of ancient oxygenation. Earth and Planetary Science Letters 547.

Bonnand, P., Boyet, M., Bosq, C., 2023. Stable cerium isotopes as a tracer of oxidation reactions. Geochem. Perspect. Lett. 28, 27–30.

Borst, A.M., Smith, M.P., Finch, A.A., Estrade, G., Villanova-de-Benavent, C., Nason, P., Marquis, E., Horsburgh, N.J., Goodenough, K.M., Xu, C., Kynicky, J., Geraki, K., 2020. Adsorption of rare earth elements in regolith-hosted clay deposits. Nat. Commun. 11 (1), 4386.

Bothamy, N., Galy, A., 2021. Industrially purified Nd materials identified by distinct mass-dependent isotopic composition. Front. Environ. Chem. 2.

Brix, P., Hüfner, S., Kienle, P., Quitmann, D., 1964. Isomer shift on Eu151. Phys. Lett. 13 (2), 140–142.

Brugger, J., Liu, W., Etschmann, B., Mei, Y., Sherman, D.M., Testemale, D., 2016. A review of the coordination chemistry of hydrothermal systems, or do coordination changes make ore deposits? Chem. Geol. 447, 219–253.

Buchachenko, A.L., 2013. Mass-independent isotope effects. J. Phys. Chem. B 117 (8), 2231–2238.

Christiansen, P.A., Ermler, W.C., Pitzer, K.S., 1985. Relativistic effects in chemical systems. Ann. Rev. Phys. Chem. 36 (1), 407–432.

Clark, A.E., 2008. Density functional and basis set dependence of hydrated Ln(III) properties. J. Chem. Theory Comput. 4 (5), 708–718.

Clavaguera, C., Pollet, R., Soudan, J.M., Brenner, V., Dognon, J.P., 2005. Molecular dynamics study of the hydration of lanthanum(III) and europium(III) including many-body effects. J. Phys. Chem. B 109 (16), 7614–7616.

Coey, J.M.D., 1976. $^{149}Sm^{3+}$ isomer shifts. J. Inorg. Nucl. Chem. 38 (6), 1139–1140.

Cosentino, U., Villa, A., Pitea, D., Moro, G., Barone, V., 2000. Extension of computational chemistry to the study of lanthanide(III) ions in aqueous solution: implementation and validation of a continuum solvent approach. J. Phys. Chem. B 104 (33), 8001–8007.

Danielson, A., Möller, P., Dulski, P., 1992. The europium anomalies in banded iron formations and the thermal history of the oceanic crust. Chem. Geol. 97 (1–2), 89–100.

Diaz-Moreno, S., Ramos, S., Bowron, D.T., 2011. Solvation structure and ion complexation of La^{3+} in a 1 molal aqueous solution of lanthanum chloride. J. Phys. Chem A 115 (24), 6575–6581.

Diehl, A., Bach, W., 2020. MARHYS (MARine HYdrothermal Solutions) database: a global compilation of marine hydrothermal vent fluid, end member, and seawater compositions. Geochem. Geophys. Geosyst. 21 (12).

Dolg, M., Stoll, H., Preuss, H., 1989. Energy-adjustedabinitiopseudopotentials for the rare earth elements. J. Chem. Phys. 90 (3), 1730–1734.

Ducher, M., Blanchard, M., Balan, E., 2016. Equilibrium zinc isotope fractionation in Zn-bearing minerals from first-principles calculations. Chem. Geol. 443, 87–96.

Eibschütz, M., Cohen, R.L., Buehler, E., Wernick, J.H., 1972. Mössbauer isomer shifts in Sm^{149} compounds. Phys. Rev. B 6 (1), 18–23.

Elderfield, H., 1997. The oceanic chemistry of the rare-earth elements. Philos. Trans. Royal Soc. London. Ser. A, Math. Phys. Sci. 325 (1583), 105–126.

Fujii, T., Moynier, F., Albarède, F., 2009. The nuclear field shift effect in chemical exchange reactions. Chem.ical Geology 267 (3–4), 139–156.

Fujii, T., Moynier, F., Agranier, A., Ponzevera, E., Abe, M., Uehara, A., Yamana, H., 2012. Nuclear field shift effect in isotope fractionation of thallium. J. Radioanal. Nucl. Chem. 296 (1), 261–265.

Fujii, T., Moynier, F., Blichert-Toft, J., Albarède, F., 2014. Density functional theory estimation of isotope fractionation of Fe, Ni, Cu, and Zn among species relevant to geochemical and biological environments. Geochim. Cosmochim. Acta 140, 553–576.

Fujii, T., Kato, C., Wada, N., Uehara, A., Sossi, P., Moynier, F., 2023. Theoretical and experimental study on vanadium isotope fractionation among species relevant to geochemistry. ACS Earth Space Chem. 7 (4), 912–925.

German, C.R., Elderfield, H., 1990. Application of the Ce anomaly as a paleoredox indicator: The ground rules. Paleoceanography 5 (5), 823–833.

Gerth, G., Kienle, P., Luchner, K., 1968. Chemical effects on the isomer shift in ^{151}Eu. Phys. Lett. A 27 (8), 557–558.

Gomes, A.S.P., Dyall, K.G., Visscher, L., 2010. Relativistic double-zeta, triple-zeta, and quadruple-zeta basis sets for the lanthanides La–Lu. Theor. Chem. Acc. 127 (4), 369–381.

Grigoriew, H., Siekierski, S., 2002. Model of short-range order in a concentrated lanthanum trichloride aqueous solution from x-ray diffraction studies. J. Phys. Chem. 97 (20), 5400–5402.

Guan, Q., Mei, Y., Etschmann, B., Louvel, M., Testemale, D., Spezia, R., Brugger, J., 2022. Speciation and thermodynamic properties of La(III)-Cl complexes in hydrothermal fluids: A combined molecular dynamics and in situ X-ray absorption spectroscopy study. Geochim. Cosmochim. Acta 330, 27–46.

Haas, J.R., Shock, E.L., Sassani, D.C., 1995. Rare earth elements in hydrothermal systems: Estimates of standard partial molal thermodynamic properties of aqueous complexes of the rare earth elements at high pressures and temperatures. Geochim. Cosmochim. Acta 59 (21), 4329–4350.

Habenschuss, A., Spedding, F.H., 1979. The coordination (hydration) of rare earth ions in aqueous chloride solutions from x-ray diffraction. II. $LaCl_3$, $PrCl_3$, and $NdCl_3$. J. Chem. Phys. 70 (8), 3758–3763.

Hanwell, M.D., Curtis, D.E., Lonie, D.C., Vandermeersch, T., Zurek, E., Hutchison, G.R., 2012. Avogadro: an advanced semantic chemical editor, visualization, and analysis platform. J Cheminform 4 (1), 17.

Hay, P.J., Wadt, W.R., 1985. Ab initio effective core potentials for molecular calculations. Potentials for K to Au including the outermost core orbitals. J. Chem. Phys. 82 (1), 299–310.

Hehre, W.J., Ditchfield, R., Pople, J.A., 1972. Self—consistent molecular orbital methods. XII. Further extensions of Gaussian—type basis sets for use in molecular orbital studies of organic molecules. J. Chem. Phys. 56 (5), 2257–2261.

Hu, J.Y., Dauphas, N., Tissot, F.L.H., Yokochi, R., Ireland, T.J., Zhang, Z., Davis, A.M., Ciesla, F.J., Grossman, L., Charlier, B.L.A., Roskosz, M., Alp, E.E., Hu, M.Y., Zhao, J., 2021. Heating events in the nascent solar system recorded by rare earth element isotopic fractionation in refractory inclusions. Sci. Adv. 7 (2).

Hu, J.Y., Tissot, F.L.H., Yokochi, R., Ireland, T.J., Dauphas, N., Williams, H.M., 2023. Determination of rare earth element isotopic compositions using sample-standard bracketing and double-spike approaches. ACS Earth Space Chem. 7 (11), 2222–2238.

Ishiguro, S., Umebayashi, Y., Komiya, M., 2002. Thermodynamic and structural aspects on the solvation steric effect of lanthanide(III)—dependence on the ionic size. Coord. Chem. Rev. 226 (1–2), 103–111.

Johansson, G., 1992. Structures of complexes in solution derived from X-ray diffraction measurements, pp. 159-232.

Jowitt, S.M., Wong, V.N.L., Wilson, S.A., Gore, O., 2017. Critical metals in the critical zone: controls, resources and future prospectivity of regolith-hosted rare earth elements. Aust. J. Earth Sci. 64 (8), 1045–1054.

Kato, Y., Yamaguchi, K.E., Ohmoto, H., 2006. Rare earth elements in Precambrian banded iron formations: Secular changes of Ce and Eu anomalies and evolution of atmospheric oxygen, Evolution of Early Earth's Atmosphere, Hydrosphere, and Biosphere - Constraints from Ore Deposits.

Lacan, F., Jeandel, C., 2005. Neodymium isotopes as a new tool for quantifying exchange fluxes at the continent–ocean interface. Earth Planet. Sci. Lett. 232 (3–4), 245–257.

Li, M.Y.H., Kwong, H.T., Williams-Jones, A.E., Zhou, M.-F., 2022. The thermodynamics of rare earth element liberation, mobilization and supergene enrichment during groundwater-regolith interaction. Geochim. Cosmochim. Acta 330, 258–277.

Li, W., Liu, X.-M., Nakada, R., Takahashi, Y., Hu, Y., Shakouri, M., Zhang, Z., Okumura, T., Yamada, S., 2023a. The cerium isotope fingerprints of redox fluctuation in bauxites. Earth and Planetary Science Letters 602.

Li, W., Nakada, R., Takahashi, Y., Gaschnig, R.M., Hu, Y., Shakouri, M., Rudnick, R.L., Liu, X.-M., 2023b. Cerium geochemical composition of the upper continental crust through time: Implications for tracing past surface redox conditions. Geochim. Cosmochim. Acta.
Li, X., Zhao, H., Tang, M., Liu, Y., 2009. Theoretical prediction for several important equilibrium Ge isotope fractionation factors and geological implications. Earth Planet. Sci. Lett. 287 (1–2), 1–11.
Liang, X., Wu, P., Wei, G., Yang, Y., Ji, S., Ma, L., Zhou, J., Tan, W., Zhu, J., Takahashi, Y., 2024. Enrichment and fractionation of rare earth elements (REEs) in ion-adsorption-type REE deposits: Constraints of an iron (hydr)oxide–clay mineral composite. Am. Mineral.: J. Earth Planet. Mater.
Liu, F., Ling, M., Zhang, Z., Lu, W., Xu, J., Li, X., Yang, D., Wu, J., Yang, H., 2023. Stable cerium isotope analysis of geological materials by MC-ICP-MS. Chem. Geol.
Liu, X., Wei, G., Zou, J., Guo, Y., Ma, J., Chen, X., Liu, Y., Chen, J., Li, H., Zeng, T., 2018. Elemental and Sr-Nd isotope geochemistry of sinking particles in the Northern South China sea: implications for provenance and transportation. J. Geophys. Res. Oceans 123 (12), 9137–9155.
Mayanovic, R.A., Anderson, A.J., Bassett, W.A., Chou, I.M., 2009. The structure and stability of aqueous rare-earth elements in hydrothermal fluids: New results on neodymium(III) aqua and chloroaqua complexes in aqueous solutions to 500 °C and 520 MPa. Chem. Geol. 259 (1–2), 30–38.
McCoy-West, A.J., Millet, M.-A., Burton, K.W., 2017. The neodymium stable isotope composition of the silicate Earth and chondrites. Earth Planet. Sci. Lett. 480, 121–132.
McCoy-West, A.J., Millet, M.-A., Burton, K.W., 2020a. The neodymium stable isotope composition of the oceanic crust: reconciling the mismatch between erupted mid-ocean ridge basalts and lower crustal gabbros. Frontiers in Earth Science 8.
McCoy-West, A.J., Millet, M.-A., Nowell, G.M., Nebel, O., Burton, K.W., 2020b. Simultaneous measurement of neodymium stable and radiogenic isotopes from a single aliquot using a double spike. J. Anal. At. Spectrom 35 (2), 388–402.
McCoy-West, A.J., Burton, K.W., Millet, M.-A., Cawood, P.A., 2021. The chondritic neodymium stable isotope composition of the Earth inferred from mid-ocean ridge, ocean island and arc basalts. Geochim. Cosmochim. Acta 293, 575–597.
McCoy-West, A.J., Mortimer, N., Burton, K.W., Ireland, T.R., Cawood, P.A., 2022. Re-initiation of plutonism at the Gondwana margin after a magmatic hiatus: The bimodal Permian-Triassic Longwood Suite, New Zealand. Gondwana Research 105, 432–449.
Meija, J., Coplen, T.B., Berglund, M., Brand, W.A., De Bièvre, P., Gröning, M., Holden, N. E., Irrgeher, J., Loss, R.D., Walczyk, T., Prohaska, T., 2016. Isotopic compositions of the elements 2013 (IUPAC Technical Report). Pure Appl. Chem. 88 (3), 293–306.
Migdisov, A.A., Williams-Jones, A.E., 2014. Hydrothermal transport and deposition of the rare earth elements by fluorine-bearing aqueous liquids. Miner. Deposita 49 (8), 987–997.
Migdisov, A., Williams-Jones, A.E., Brugger, J., Caporuscio, F.A., 2016. Hydrothermal transport, deposition, and fractionation of the REE: Experimental data and thermodynamic calculations. Chem. Geol. 439, 13–42.
Momma, K., Izumi, F., 2011. VESTA 3 for three-dimensional visualization of crystal, volumetric and morphology data. J. Appl. Cryst. 44 (6), 1272–1276.
Moynier, F., Fujii, T., Shaw, A.S., Le Borgne, M., 2013. Heterogeneous distribution of natural zinc isotopes in mice. Metallomics 5 (6), 693–699.
Nakada, R., Takahashi, Y., Tanimizu, M., 2013a. Isotopic and speciation study on cerium during its solid–water distribution with implication for Ce stable isotope as a paleo-redox proxy. Geochim. Cosmochim. Acta 103, 49–62.
Nakada, R., Tanimizu, M., Takahashi, Y., 2013b. Difference in the stable isotopic fractionations of Ce, Nd, and Sm during adsorption on iron and manganese oxides and its interpretation based on their local structures. Geochim. Cosmochim. Acta 121, 105–119.
Nakada, R., Takahashi, Y., Tanimizu, M., 2016. Cerium stable isotope ratios in ferromanganese deposits and their potential as a paleo-redox proxy. Geochim. Cosmochim. Acta 181, 89–100.
Nakada, R., Tanaka, M., Tanimizu, M., Takahashi, Y., 2017. Aqueous speciation is likely to control the stable isotopic fractionation of cerium at varying pH. Geochim. Cosmochim. Acta 218, 273–290.
Narten, A.H., Hahn, R.L., 2002. Hydration of the neodymium(3+) ion in neodymium chloride solutions determined by neutron diffraction. J. Phys. Chem. 87 (17), 3193–3197.
Naslund, J., Lindqvist-Reis, P., Persson, I., Sandstrom, M., 2000. Steric effects control the structure of the solvated lanthanum(III) ion in aqueous, dimethyl sulfoxide, and N, N'-dimethylpropyleneurea solution. An EXAFS and large-angle X-ray scattering study. Inorg. Chem. 39 (18), 4006–4011.
Neese, F., 2003. An improvement of the resolution of the identity approximation for the formation of the Coulomb matrix. J. Comput. Chem. 24 (14), 1740–1747.
Neese, F., 2011. The ORCA program system. WIREs Comput. Mol. Sci. 2 (1), 73–78.
Ni, Y., Hughes, J.M., Mariano, A.N., 1995. Crystal chemistry of the monazite and xenotime structures. Am. Mineral. 80 (1–2), 21–26.
O'Neil, J.R., 1986. Theoretical and experimental aspects of isotopic fractionation. Rev. Mineral. 16, 1–40.
Parkhurst, D.L., Appelo, C.A.J., 2013. Description of input and examples for PHREEQC version 3: a computer program for speciation, batch-reaction, one-dimensional transport, and inverse geochemical calculations.
Pease, V., Rollinson, H., 2021. Using Geochemical Data: To Understand Geological Processes. Cambridge University Press, Cambridge.
Persson, I., D'Angelo, P., De Panfilis, S., Sandstrom, M., Eriksson, L., 2008. Hydration of lanthanoid(III) ions in aqueous solution and crystalline hydrates studied by EXAFS spectroscopy and crystallography: the myth of the "gadolinium break". Chemistry 14 (10), 3056–3066.
Petit, L., Vuilleumier, R., Maldivi, P., Adamo, C., 2008. Molecular dynamics study of the coordination sphere of trivalent lanthanum in a highly concentrated LiCl aqueous solution: a combined classical and ab initio approach. J. Phys. Chem. B 112 (34), 10603–10607.
Pourkhorsandi, H., Debaille, V., de Jong, J., Armytage, R.M.G., 2021. Cerium stable isotope analysis of synthetic and terrestrial rock reference materials by MC-ICPMS. Talanta 224, 121877.
Roy, L.E., Hay, P.J., Martin, R.L., 2008. Revised basis sets for the LANL effective core potentials. J. Chem. Theory Comput. 4 (7), 1029–1031.
Rudolph, W.W., Irmer, G., 2020. On the hydration of the rare earth ions in aqueous solution. J. Solut. Chem. 49 (3), 316–331.
Sanematsu, K., Watanabe, Y., Verplanck, P.L., Hitzman, M.W., 2016. Characteristics and genesis of ion adsorption-type rare earth element deposits, rare earth and critical elements in ore deposits. Soc. Econ. Geol., p. 0.
Saue, T., Bast, R., Gomes, A.S.P., Jensen, H.J.A., Visscher, L., Aucar, I.A., Di Remigio, R., Dyall, K.G., Eliav, E., Fasshauer, E., Fleig, T., Halbert, L., Hedegard, E.D., Helmich-Paris, B., Ilias, M., Jacob, C.R., Knecht, S., Laerdahl, J.K., Vidal, M.L., Nayak, M.K., Olejniczak, M., Olsen, J.M.H., Pernpointner, M., Senjean, B., Shee, A., Sunaga, A., van Stralen, J.N.P., 2020. The DIRAC code for relativistic molecular calculations. J. Chem. Phys. 152 (20), 204104.
Schauble, E.A., 2004. Applying stable isotope fractionation theory to new systems. Rev. Mineral. Geochem. 55 (1), 65–111.
Schauble, E.A., 2011. First-principles estimates of equilibrium magnesium isotope fractionation in silicate, oxide, carbonate and hexaaquamagnesium(2+) crystals. Geochim. Cosmochim. Acta 75 (3), 844–869.
Schauble, E.A., 2023. Nuclear volume isotope fractionation of europium and other lanthanide elements. Geochem. J. 57 (4), 118–133.
Sherman, D.M., 2013. Equilibrium isotopic fractionation of copper during oxidation/reduction, aqueous complexation and ore-forming processes: Predictions from hybrid density functional theory. Geochim. Cosmochim. Acta 118, 85–97.
Sholkovitz, E.R., Landing, W.M., Lewis, B.L., 1994. Ocean particle chemistry: The fractionation of rare earth elements between suspended particles and seawater. Geochim. Cosmochim. Acta 58 (6), 1567–1579.
Solera, J.A., Garcia, J., Proietti, M.G., 1995. Multielectron excitations at the L edges in rare-earth ionic aqueous solutions. Phys. Rev. B Condens. Matter 51 (5), 2678–2686.
Stumm, W., 1987. Aquatic surface chemistry : chemical processes at the particle-water interface. Wiley, New York.
Stumm, W., Morgan, J.J., 1995. Aquatic chemistry : chemical equilibria and rates in natural waters, 3rd ed. Wiley, New York.
Sun, Z., Cao, H., Yin, X., Zhang, X., Dong, A., Liu, L., Geng, W., 2018. Precipitation and subsequent preservation of hydrothermal Fe-Mn oxides in distal plume sediments on Juan de Fuca Ridge. J. Mar. Syst. 187, 128–140.
Tang, J., Johannesson, K.H., 2010. Rare earth elements adsorption onto Carrizo sand: Influence of strong solution complexation. Chemical Geology 279 (3–4), 120–133.
Tostevin, R., 2021. Cerium Anomalies and Paleoredox.
Turekian, K.K., 1977. The fate of metals in the oceans. Geochim. Cosmochim. Acta 41 (8), 1139–1144.
Urey, H.C., 1947. The thermodynamic properties of isotopic substances. J. Chem. Soc. 562–581.
Vance, D., Burton, K., 1999. Neodymium isotopes in planktonic foraminifera: a record of the response of continental weathering and ocean circulation rates to climate change. Earth Planet. Sci. Lett. 173 (4), 365–379.
Visscher, L., Dyall, K.G., 1997. Dirac-Fock atomic electronic structure calculations using different nuclear charge distributions. At. Data Nucl. Data Tables 67 (2), 207–224.
Weigend, F., 2006. Accurate Coulomb-fitting basis sets for H to Rn. PCCP 8 (9), 1057–1065.
Weigend, F., Ahlrichs, R., 2005. Balanced basis sets of split valence, triple zeta valence and quadruple zeta valence quality for H to Rn: Design and assessment of accuracy. PCCP 7 (18), 3297–3305.
Wiederhold, J.G., Cramer, C.J., Daniel, K., Infante, I., Bourdon, B., Kretzschmar, R., 2010. Equilibrium mercury isotope fractionation between dissolved Hg(II) species and thiol-bound Hg. Environ. Sci. Tech. 44 (11), 4191–4197.
Wilkinson, J.J., Weiss, D.J., Mason, T.F.D., Coles, B.J., 2005. Zinc isotope variation in hydrothermal systems: preliminary evidence from the irish midlands ore field. Econ. Geol. 100 (3), 583–590.
Yamaguchi, T., Nomura, M., Wakita, H., Ohtaki, H., 1988. An extended x-ray absorption fine structure study of aqueous rare earth perchlorate solutions in liquid and glassy states. J. Chem. Phys. 89 (8), 5153–5159.
Yang, J., Li, Y., Liu, S., Tian, H., Chen, C., Liu, J., Shi, Y., 2015. Theoretical calculations of Cd isotope fractionation in hydrothermal fluids. Chem. Geol. 391, 74–82.
Yang, M., Liang, X., Ma, L., Huang, J., He, H., Zhu, J., 2019. Adsorption of REEs on kaolinite and halloysite: A link to the REE distribution on clays in the weathering crust of granite. Chem. Geol. 525, 210–217.
Yang, S., Liu, Y., 2016. Nuclear field shift effects on stable isotope fractionation: a review. Acta Geochimica 35 (3), 227–239.
Zhang, J., Shi, R., 2022. Theoretical Calculation of Equilibrium Cadmium Isotope Fractionation Factors between Cadmium-bearing sulfides and aqueous solutions. Geochem. J. 56 (6), 180–196.
Zhang, W., Yan, T., 2022. A molecular dynamics investigation of La^{3+} and Lu^{3+}-ligand speciation in aqueous solution. J. Mol. Liq. 347.
Zhao, Y., Li, Y., Wiggenhauser, M., Yang, J., Sarret, G., Cheng, Q., Liu, J., Shi, Y., 2021. Theoretical isotope fractionation of cadmium during complexation with organic ligands. Chem. Geol. 571.